

# Phase transitions of a 2D deformed-AKLT model

Nicholas Pomata,<sup>1</sup> Ching-Yu Huang,<sup>1,2</sup> and Tzu-Chieh Wei<sup>1</sup>

<sup>1</sup>*C. N. Yang Institute for Theoretical Physics and Department of Physics and Astronomy,  
State University of New York at Stony Brook, NY 11794-3840, United States*

<sup>2</sup>*Physics Division, National Center for Theoretical Science, Hsinchu 30013, Taiwan*

(Dated: March 9, 2022)

We study spin-2 deformed-AKLT models on the square lattice, specifically a two-parameter family of  $O(2)$ -symmetric ground-state wavefunctions as defined by Niggemann, Klümper, and Zittartz, who found previously that the phase diagram consists of a Néel-ordered phase and a disordered phase which contains the AKLT point. Using tensor-network methods, we not only confirm the Néel phase but also find an XY phase with quasi-long-range order and a region adjacent to it, within the AKLT phase, with very large correlation length, and investigate the consequences of a perfectly-factorizable point at the corner of that phase.

## I. INTRODUCTION

Haldane's prediction concerning the finite spectral gap of the 1D integer-spin antiferromagnetic Heisenberg chain and its featureless ground state was quite unexpected<sup>1</sup>, as it seemed incompatible with the theorem of Lieb, Schultz and Mattis<sup>2</sup> on half-integer spin chains, with the difference coming from the presence or absence of a topological  $\theta$  term. In order to understand the integer-spin case, Affleck, Kennedy, Lieb and Tasaki (AKLT) constructed a state which admits no local order parameter and which is the exact ground state of a Hamiltonian whose finite gap can be proven rigorously.<sup>3,4</sup> Their construction, which used valence bonds, was then generalized to two dimensions, for example on the honeycomb and square lattices. Recently, these two-dimensional valence-bond AKLT states and parent Hamiltonians have also been recognized as examples of systems with weak symmetry-protected topological order<sup>5-7</sup>, and, somewhat unexpectedly, as a means to realize universal quantum computation in a measurement-based approach.<sup>8,9</sup>

Here we study a two-parameter family of wave functions on the square lattice as constructed by Niggemann, Klümper, and Zittartz (NKZ)<sup>10</sup> and investigate the corresponding phase diagram. These wave functions, which contain the AKLT state as a special case, are ground states of a class of two-site interacting frustration-free spin-2 Hamiltonians on the square lattice, which have spin-flip and rotation symmetry in the  $z$  direction and are symmetric under lattice rotations, translations, and reflections.<sup>10</sup> We shall refer to these states as the "deformed-AKLT" family of states, as they may be obtained by applying an on-site deformation to the AKLT state.

In their original work, through a combination of Monte-Carlo analysis and approximation by an exactly-solvable classical model, Niggemann, Klümper, and Zittartz predicted that an Ising-like transition divides the two-parameter phase diagram into a Néel-ordered phase and a disordered phase. This matches their result for the spin- $\frac{3}{2}$  model, which Hieida et al.<sup>11</sup> further confirmed

by applying a progenitor of the CTMRG approach that we describe in Appendix A 1. As in the preceding work by Huang, Wagner, and Wei<sup>12</sup>, we apply tensor-network analyses to this system in order to better understand and characterize these phases. In addition, following the evidence for an XY-like phase in that work, we seek to determine whether or not the disordered "phase" further divides into multiple phases, which we strongly expect to find since the disordered region of the phase diagram contains both the AKLT point, which possesses symmetry-protected topological (SPT) order, in its interior, and a product state at its boundary.

Among the phases, the ordered phase can be easily characterized by spontaneous symmetry breaking using a staggered  $S_z$  as a local order parameter; as this order parameter can be directly calculated by tensor-network methods, we can accurately locate the boundary between this phase and the AKLT phase. For the featureless valence-bond AKLT phase, we can use simulated modular  $S$  and  $T$  matrices to distinguish its SPT order from other phases.<sup>13-15</sup> We also isolate, in a region surrounding the product-state point at the origin of the parameter space, a critical phase with distinctive properties that we can examine in terms of the conformal field theory of the classical XY model. By doing so we reveal robust evidence for the existence of such a phase and for a Kosterlitz-Thouless transition between it and the SPT-ordered AKLT phase. This is in contrast to the spin-3/2 case<sup>12</sup>, which new evidence presented in Sec. IV suggests does not contain a truly critical, or quasi-long-range ordered, XY phase, but instead only has a region of very long correlation length. Such pseudo-quasi-long-range order also exists on the square lattice, in a region of the AKLT phase adjacent to the true XY phase. Its existence is related to the suppression of  $S_z = \pm 2$  components in this region, resulting in approximate spin-1 behavior for which the Berry phase from the topological  $\theta$  term almost suppresses isolated tunneling processes.<sup>16</sup>

We also examine the possibility of a third disordered phase, a trivial phase adiabatically connected to the product state at the origin  $a_1 = a_2 = 0$  of the two-parameter space (as shown in Fig. 1). With any single

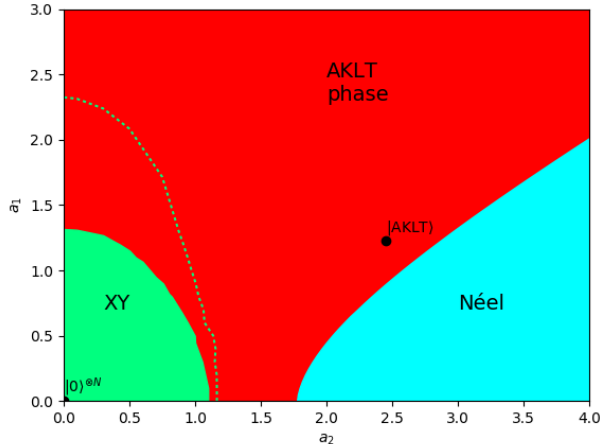


FIG. 1. The phase diagram of the square-lattice deformed-AKLT model with deformation parameterized by  $a_2$  and  $a_1$  as given in (3). Néel indicates the Néel-ordered phase, with boundary determined as in Fig. 6; XY indicates the XY-like phase with quasi-long-range order, with boundary estimated by interpolating from the data in Fig. 9b; and AKLT indicates the AKLT phase, with the isotropic AKLT point indicated as  $|\text{AKLT}\rangle$ . Likewise the product state at the origin of parameter space is noted as  $|0^{\otimes N}\rangle$ . The green dotted line demarks the pseudo-quasi-long-range-ordered region; points on this line have correlation length  $\xi \sim 10^3$  estimated from TNR data by interpolating the parameter where the classical central charge takes the value  $c \simeq 0.35$  after 10 RG steps, as indicated by Fig. 14.

fixed bond-dimension sweep of the phase diagram, we find that the trivial phase occupies only a very small region near the origin; as we increase the bond dimension of the tensor-network algorithm being used, we find that that region shrinks, suggesting that this “phase” might not be anything more than an isolated point in the phase diagram.

In Sec. II, we begin by describing the family of states we will be working with and their inherent properties, in addition to how tensor-network algorithms can apply to them. Then in Sec. III we will describe the phases that we expect to find in the phase diagram of the system on the square lattice, and detail our results, as obtained using the tensor-network renormalization (TNR) and higher-order tensor renormalization group (HOTRG) methods and summarized in the phase diagram in Fig. 1. Finally, in Sec. IV, we return to the honeycomb lattice to re-evaluate the evidence for the XY phase there.

## II. THE VALENCE-BOND STATE

To define the deformed-AKLT state, we write a general AKLT state, which will be a tensor-network state with bond dimension  $\chi = 2$  on an arbitrary lattice and introduce a continuously-parameterized deformation.

We start with some lattice with coordination number  $q$ . On each link we place a state of two spin- $\frac{1}{2}$  virtual spins such that each vertex has  $q$  such spins. We then produce the physical degree of freedom by applying a projector  $\mathbb{P}_q$  from the  $q$  spins  $|\eta_i\rangle$  onto the spin- $q/2$  subspace:

$$\mathbb{P}_q = \sum_{\eta_1, \eta_2, \dots, \eta_q} c_s |s\rangle \langle \eta_1, \eta_2, \dots, \eta_q|, \quad (1)$$

where  $s = \sum_i \eta_i$  is the physical index,  $\eta_i = \pm \frac{1}{2}$  represent the virtual spins in their  $S_z$  basis, and  $c_s$  are Clebsch-Gordan coefficients. This yields the AKLT state

$$|\psi_{\text{AKLT}}\rangle = \bigotimes_{v \in V} (\mathbb{P}_q)_v \bigotimes_{l \in L} |\psi^-\rangle_l, \quad (2)$$

where the singlet states  $|\psi^-\rangle = |\uparrow\downarrow\rangle - |\downarrow\uparrow\rangle$  are placed on every link  $l$  of the lattice.

We then apply a diagonal, spin-flip-invariant deformation

$$D(\vec{a}) = \sum_{s=-q/2}^{q/2} \frac{a_{|s|}}{c_s} |s\rangle \langle s| \quad (3)$$

in the  $S^z$  basis to the physical indices. Then we arrive at a family of deformed-AKLT states,

$$|\Psi(\vec{a})_{\text{deformed}}\rangle \propto D(\vec{a})^{\otimes N} |\psi_{\text{AKLT}}\rangle. \quad (4)$$

For the remainder of this work, we will fix  $a_0 = 1$  (or  $a_{\frac{1}{2}} = 1$  for half-integer-spin cases). We thus, for example, end up with two independent parameters in the spin-2 case and only one independent parameter in the spin-3/2 case.

In short, the deformed-AKLT family of wave functions can be written as

$$|\Psi(\vec{a})_{\text{deformed}}\rangle = \bigotimes_{v \in V} (D(\vec{a})\mathbb{P}_q)_v \bigotimes_{l \in L} |\psi^-\rangle_l, \quad (5)$$

where the operator  $D(\vec{a})\mathbb{P}_q$  maps the virtual spaces (which represent the entanglement between the virtual spins) at each vertex  $v$  to the physical space.

We can modify the original two-site AKLT Hamiltonian<sup>17</sup> to obtain a parent Hamiltonian which locally annihilates this state:

$$H(\vec{a}) \equiv \sum_{\langle i,j \rangle} D(\vec{a})_i^{-1} \otimes D(\vec{a})_j^{-1} h_{ij}^{(\text{AKLT})} D(\vec{a})_i^{-1} \otimes D(\vec{a})_j^{-1}, \quad (6)$$

$$h_{ij}^{(\text{AKLT})} \equiv \frac{1}{28} \left( S_{ij} + \frac{7}{10} S_{ij}^2 + \frac{7}{45} S_{ij}^3 + \frac{1}{90} S_{ij}^4 \right)$$

$$S_{ij} \equiv \vec{S}_i \cdot \vec{S}_j$$

As  $h_{ij}^{(\text{AKLT})}$  annihilates the AKLT state, it follows that  $H(\vec{a})$  annihilates the deformed AKLT state.

Additionally, Niggeman, Klümper, and Zittartz constructed a more general, five-parameter family of two-site, frustration-free Hamiltonians, invariant under lattice symmetries as well as on-site spin-flip and  $S_z$  invariance. We note however that the above Hamiltonian is not well-defined when any component  $a_i$  of  $\vec{a}$  is zero (under which circumstance we would need to increase the rank of the two-site Hamiltonian - impossible with a continuous deformation). We shall also consider below AKLT-like states constructed using maximally-entangled two-qubit states other than  $|\psi^-\rangle$  as the valence bonds.

### A. Tensor network representation, bond states, and symmetry

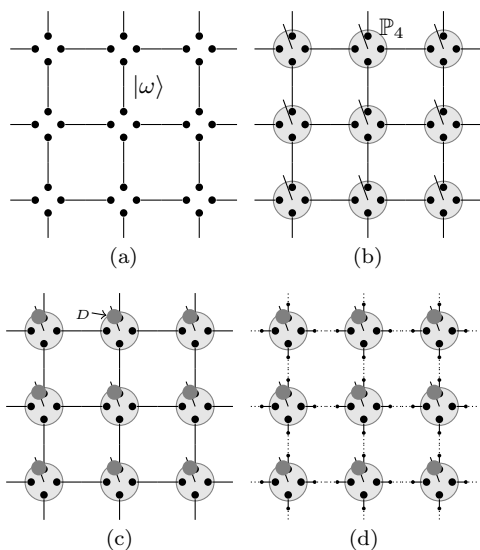


FIG. 2. The valence-bond state and tensor-network state pictures of the spin-2 deformed-AKLT state on the square lattice. (a) A singlet state (or, more generally, a bond state  $|\omega\rangle$  composed from two virtual spin- $\frac{1}{2}$  degrees of freedom) is placed on each edge of the lattice. (b) The AKLT state is formed by placing a spin-2 projector  $\mathbb{P}_4$  on each site; the spin-2 indices of the projectors indicate the physical degrees of freedom. (c) From there the deformation  $D(\vec{a})$  is applied to each site, resulting in the deformed-AKLT state. (d) In order to represent this in the typical manner of a PEPS, we may for example perform a Schmidt decomposition on the bond states; the Schmidt indices then becomes the “bond” indices of the tensor network, and the contraction of the resulting objects and the deformation matrix with the five indices of the projection matrix yields the on-site tensor.

Given a state in the valence-bond picture we have just presented, it is natural to represent it as a tensor network state (TNS), namely a projected entangled pair state (PEPS). For those who are not familiar with tensor network states, we recommend several of the cited review and pedagogical papers<sup>18–22</sup>. In this representation we place on each lattice site a rank- $(q+1)$  tensor with

one physical index (the spin on the site) and  $q$  virtual indices (corresponding to the  $q$  virtual spins at the site, or more precisely their Schmidt index); pairs of virtual indices of adjacent sites are contracted over in a tensor trace (tTr) to yield the physical state. In an AKLT system we begin with a rank- $(q+1)$  tensor on each site (the projector  $\mathbb{P}_q$ ) as well as a rank-2 tensor on each link (the virtual singlets). To get a PEPS description we may assign each singlet to a neighboring site and contract it with the corresponding index of that site’s projector, although the way in which the bonds are defined is essentially a gauge choice and thus can be easily varied. From this we obtain a PEPS description of a general deformed-AKLT state by contracting the AKLT physical indices with the deformation matrix  $D(\vec{a})$ .

We may also alter the state by replacing the singlet state  $|\psi^-\rangle$  in the above description with a more general bond state  $|\omega\rangle$ . In particular we may use the Bell states

$$\begin{aligned} |\phi^+\rangle &= |\uparrow\uparrow\rangle + |\downarrow\downarrow\rangle \\ |\phi^-\rangle &= |\uparrow\uparrow\rangle - |\downarrow\downarrow\rangle = I \otimes \sigma^z |\phi^+\rangle \\ |\psi^+\rangle &= |\uparrow\downarrow\rangle + |\downarrow\uparrow\rangle = I \otimes \sigma^x |\phi^+\rangle \\ |\psi^-\rangle &= |\uparrow\downarrow\rangle - |\downarrow\uparrow\rangle = I \otimes i\sigma^y |\phi^+\rangle, \end{aligned} \quad (7)$$

where  $\sigma^k, k \in \{0, x, y, z\}$  are Pauli matrices and  $\sigma^0 = \mathbb{I}$ ; we may refer to the states  $|\phi^\pm\rangle$  as “ferromagnetic” bond states and the states  $|\psi^\pm\rangle$  as “antiferromagnetic” bond states, due to the behavior of the respective systems in the ordered regime as discussed below. This construction is shown graphically in Fig. 2.

When working on a bipartite lattice, we may change from one such bond state to another by applying  $SU(2)$  transformations  $U_A$  and  $U_B$  which commute with the deformation  $D(\vec{a})$  to all of the sites of the sublattices  $A$  and  $B$ , respectively. Due to the  $SU(2)$ -invariance of the projector  $\mathbb{P}_q$ , this is equivalent to performing the transformation  $|\omega\rangle \mapsto U_A^{(1/2)} \otimes U_B^{(1/2)} |\omega\rangle$  to every bond state. Therefore, if we start with the singlet  $|\psi^-\rangle$  as our bond state, we may then convert it to

- i  $|\phi^+\rangle$  by applying  $U_A = R_y^{-\frac{\pi}{2}}$  and  $U_B = R_y^{\frac{\pi}{2}}$  to the  $A$  and  $B$  sublattices, respectively;
- ii  $|\phi^-\rangle$  by applying  $U_A = R_x^{-\frac{\pi}{2}}$  and  $U_B = R_x^{\frac{\pi}{2}}$ ; and
- iii  $|\psi^+\rangle$  by applying  $U_A = R_z^{-\frac{\pi}{2}}$  and  $U_B = R_z^{\frac{\pi}{2}}$ ,

where the  $SU(2)$  rotation  $R_j^\phi \equiv e^{-i\phi S_j}$ . Thus, given physical data from any of these four systems, we may easily produce the corresponding information about any of the other. If for example we find it simpler to manipulate the tensors we use in the case  $|\omega\rangle = |\phi^+\rangle$ , we can apply any conclusions we draw about that case, such as boundaries of phase diagrams, to the more standard case of  $|\omega\rangle = |\psi^-\rangle$ .

However, on a lattice which is not bipartite, this mapping is not generally possible; in fact only the  $\phi^+$  and

$\phi^-$  bond states can be identified with each other (by applying  $R_z^{\frac{\pi}{2}}$  to every site), and we expect in general to get three distinct phase diagrams from these four bond states.

As both the tensors used to build the AKLT state, that is the projector  $\mathbb{P}_q$  and the singlet state  $\psi^-$ , are invariant under  $SU(2)$  transformations, the state itself maintains a global  $SU(2)$  invariance. However, the deformation  $D(\bar{a})$  breaks this symmetry down to a subgroup isomorphic to  $O(2)$  which can be characterized by its action on the  $xy$  plane, on which rotations are generated by  $S_z$  and reflections are produced by spin-flips such as  $R_x^\pi = e^{\pi i S_x}$  and  $R_y^\pi = e^{\pi i S_y}$ .

Now consider states  $|\Psi_\omega\rangle$  with different bond states, obtained by applying  $U_A$  and  $U_B$  to the state  $|\Psi_{\psi^-}\rangle$ . If  $g \in O(2)$  preserves  $|\Psi_{\psi^-}\rangle$ , then  $|\Psi_\omega\rangle$  will be preserved by applying  $U_A g U_A^\dagger$  to sublattice A and  $U_B g U_B^\dagger$  to sublattice B.<sup>23</sup> For the antiferromagnetic bond state  $\psi^+$ ,  $U_A$  and  $U_B$  commute with  $U(1)$  rotations and are exchanged by  $O(2)$  reflections, so that the symmetry applied in that case will still preserve the state (assuming there are an even number of sites).

When performing numerical analysis, it may be useful, for data collection and/or for numerical stability, to explicitly preserve the global on-site symmetry<sup>24,25</sup> by ensuring that the tensors produced in each step of the renormalization procedures remain invariant. (However, due to limitations in our code as of when these data were collected, we have not preserved  $O(2)$  itself but rather some adequately large finite subgroup thereof, either  $\mathbb{Z}_2 \times \mathbb{Z}_2$ ,  $D_{40}$ , or  $D_{80}$ .)

## B. Representation as a (pseudo)classical model

Much as we have shown, a two-dimensional quantum state can often be represented as a tensor network state (TNS), whose coefficients in a fixed basis are expressed as a contraction of a tensor network, that is, a tensor trace:

$$|\psi\rangle = \sum_{s_1, s_2, \dots, s_m \dots} \text{tTr}(A^{s_1} A^{s_2} \dots A^{s_m} \dots) |s_1 s_2 \dots s_m \dots\rangle, \quad (8)$$

where  $A_{\alpha, \beta, \gamma, \dots}^s$  is a local tensor with a physical index  $s$  and internal or bond indices  $\alpha, \beta, \gamma, \dots$ , and  $\text{tTr}$  denotes tensor contraction of all the connected inner indices according to the underlying lattice structure. TNS defined on two- or higher-dimensional lattices are often referred to as PEPS.

The norm squared of a TNS is given by

$$\langle \psi | \psi \rangle = \text{tTr}(\mathbb{T}^1 \mathbb{T}^2 \mathbb{T}^3 \dots \mathbb{T}^m \dots), \quad (9)$$

where we form the local *doubled tensor*  $\mathbb{T}^i$  by merging a bra layer and a ket layer, contracting the physical indices

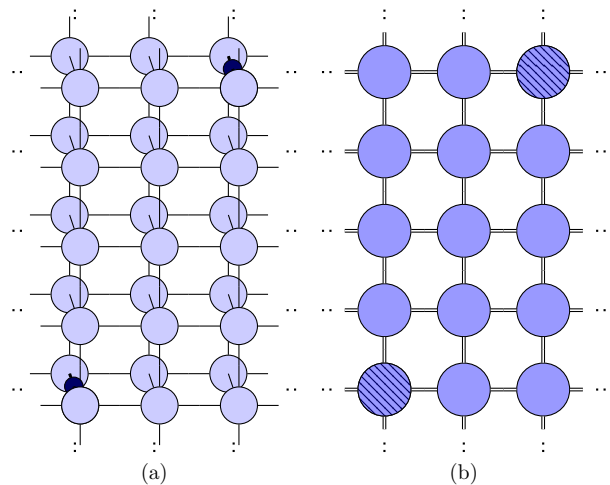


FIG. 3. Correlations in a PEPS and the corresponding representation in a classical model. (a) The correlation function  $\langle \Psi | A B | \Psi \rangle$  of two one-site operators in a quantum state  $\Psi$  represented by a PEPS. (b) The correlation function  $\langle \mathcal{O}_A \mathcal{O}_B \rangle$  of two classical “operators,” shaded, which replace the weight matrix at a site with a different tensor. In this case the classical model is the “doubled vertex model” and the operators in it are determined by contracting the quantum operator with bra and ket tensors.

of corresponding pairs of tensors  $A$  and  $A^*$ :

$$\mathbb{T} \equiv \sum_s (A_{\alpha, \beta, \gamma, \delta, \dots}^s) \times (A_{\alpha', \beta', \gamma', \delta', \dots}^{s*}). \quad (10)$$

In this way, a quantum model maps into something resembling a classical vertex model on the same lattice, in which the doubled tensor plays the role of the weight matrix in the corresponding classical model<sup>26</sup>. As in Fig. 3, we can often translate observable quantities describing the quantum state into observable quantities describing the classical model, which helps us get information about the former from the latter. We will refer to this as the “doubled vertex” model.

However, in two and higher dimensions it is in general computationally intractable to exactly calculate the tensor trace, that is, to contract the whole tensor network, for reasonably large system sizes. Several approximation schemes have been proposed as solutions in this context, such as the iPEPS algorithm<sup>18</sup>, the corner transfer matrix method (CTMRG)<sup>27,28</sup>, and coarse-graining approaches<sup>29–32</sup>, all of which tackle the contraction problem essentially by truncating information and thus scaling down the computational complexity to the polynomial level.

In Appendix A, we will discuss those methods we have used, namely the corner transfer matrix, quantum-state renormalization group, higher-order tensor renormalization group, tensor network renormalization, and loop-TNR methods.

### III. RESULTS

Here we describe how we characterize the distinct phases that appear in this two-parameter family of states, as shown in Fig. 1, and then present the numerical results arising from this analysis.

#### A. The Néel-ordered phase

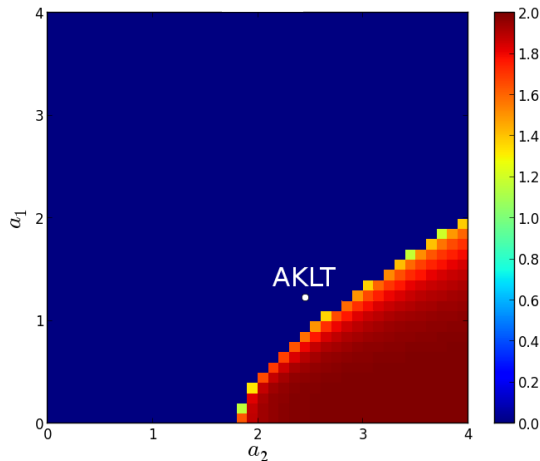


FIG. 4. Applying HOTRG with  $\chi = 40$ , and extracting the magnetization  $\langle S_z \rangle$ , we find a sharp phase transition from a disordered region (containing the AKLT, XY, and product-state phases) into an ordered region, with the magnetization rapidly increasing to 2.

In the limit  $a_2 \rightarrow \infty$  (equivalently,  $a_0, a_1 \rightarrow 0$ , where the deformation becomes a projection onto  $S_z = \pm 2$ ) the tensors  $T = Q(\vec{a})\mathbb{P}_4$  effectively become the mapping  $|2\rangle\langle\uparrow\uparrow\uparrow| + |-2\rangle\langle\downarrow\downarrow\downarrow|$ . Assuming the standard bond state  $\psi^-$ , the deformed-AKLT state will then be a cat state with two dominant configurations  $|+2, -2, \dots, +2, -2\rangle$  and  $|-2, +2, \dots, -2, +2\rangle$ . Thus, as we approach this limit we expect a phase where these states will, in the thermodynamic limit, exhibit spontaneous symmetry breaking to Néel-ordered states.

We can detect this order using the staggered order parameter  $(-1)^{n+m}S_z$ . In Fig. 4, we see that this order parameter obtains an expectation value within a well-defined region surrounding the  $a_2 \rightarrow \infty$  limit (and nowhere else).

#### B. The AKLT phase

The isotropic AKLT state is known to have nontrivial but weak symmetry-protected topological order, preserved under translations combined with on-site  $SU(2)$  transformations<sup>5-7</sup> or a suitable subgroup thereof - for

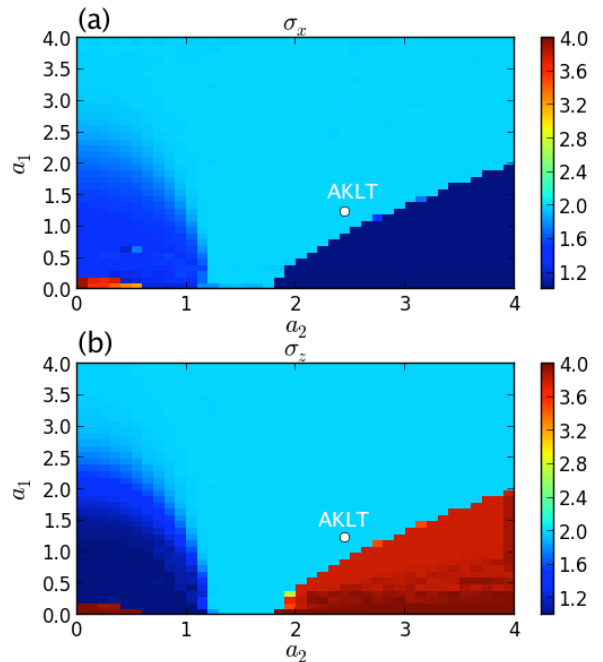


FIG. 5. The trace of the simulated modular matrix  $T$  of symmetry twists (a)  $\sigma_x$  and (b)  $\sigma_z$ , calculated using HOTRG with bond dimension  $\chi = 30$  after 10 RG steps, plotted over all the regions of the phase diagram we have studied. These quantities sharply define the AKLT-Néel phase transition, and approximately define the KT transition.

our purposes, rotations and reflections in the  $xy$  plane combining to form  $O(2)$ . As discussed in Sec. II A, the deformations we are considering commute with these symmetries, so we expect the AKLT point  $(a_2, a_1, a_0) = (\sqrt{6}, \sqrt{\frac{3}{2}}, 1)$  to be contained within a larger disordered-antiferromagnet phase behaving as a nontrivial weak SPT phase under these symmetries.

In order to detect this phase we use simulated modular matrices of Huang and Wei<sup>13,15</sup>, which originated from the idea that gauging SPT order yields intrinsic topological order<sup>14</sup>. Applying  $R_i^\pi$  to the physical index of a site tensor is equivalent to applying the Pauli matrix  $\sigma^i$  to the virtual indices. Because of this we can extract simulated  $S$  and  $T$  matrices by representing symmetry twists in the Hamiltonian with strings of  $\sigma^i$  operators applied to virtual bonds. At the AKLT point, the modular matrices arising from symmetry twists  $\sigma^x$ ,  $\sigma^y$ , or  $\sigma^z$  should be

$$S = \begin{pmatrix} 1 & 0 & 0 & 0 \\ 0 & 0 & 1 & 0 \\ 0 & 1 & 0 & 0 \\ 0 & 0 & 0 & 1 \end{pmatrix}, \quad T = \begin{pmatrix} 1 & 0 & 0 & 0 \\ 0 & 1 & 0 & 0 \\ 0 & 0 & 0 & 1 \\ 0 & 0 & 1 & 0 \end{pmatrix}, \quad (11)$$

so that  $\text{tr}(S) = \text{tr}(T) = 2$ . As we expect this to be a constant of an SPT phase, we may follow these quantities and use  $\text{tr}(T) = 2$  as an indicator of nontrivial SPT order;

when  $\text{tr}(T)$  is 1 or 4, meanwhile, we identify a trivial or symmetry-breaking phase.

In Fig. 5, we see that, in precisely the ordered region indicated by Fig. 4, the traces of the modular  $T$  matrices corresponding to each of the symmetry twists  $\sigma_x$  and  $\sigma_z$  take the trivial values of 1 and 4, respectively. In most of the disordered region, meanwhile, both of these traces equal 2, with a very sharp transition between these two regimes. Where we find  $\text{tr}(T_x) = \text{tr}(T_y) = 2$ , we are within the SPT-ordered AKLT phase. We will discuss the region in which these traces appear to continuously vary shortly.

### C. Characteristics of the transition between Néel-ordered and AKLT phases

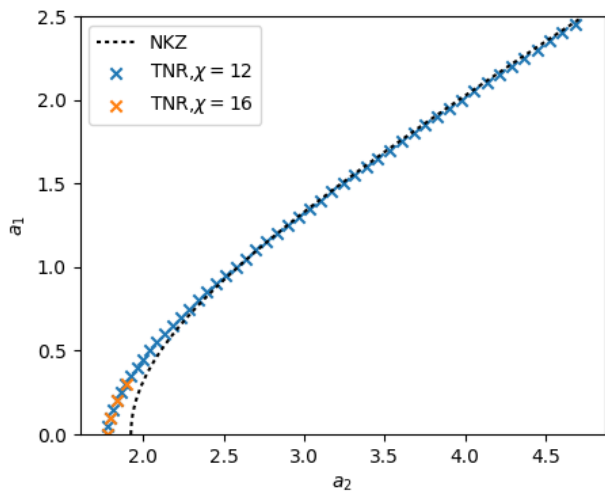


FIG. 6. The line of transition between the Néel and AKLT phases, as determined by sweeping  $a_2$  given fixed  $a_1$  with TNR for nontrivial central charge at scales of up to 12 coarse-graining steps, primarily using bond dimension  $\chi=12$ ,  $\chi'=10$  but with  $\chi=16$ ,  $\chi'=12$  for confirmation. We find reasonable agreement with the findings of NKZ in the asymptotic limit  $a_1, a_2 \rightarrow \infty$ , but for  $a_1 \rightarrow 0$  we find disagreement, confirmed by increasing bond dimension as in Table I, that exceeds their estimates of error.

The disordered and Néel-ordered phases described above were previously identified by Niggeman, Klümper, and Zittartz in their original work, using Monte-Carlo methods. They additionally claim that the critical line separating these two phases has Ising-like critical exponents and is located at  $a_2^2 = (3.0 \pm 0.1)a_1^2 + (3.7 \pm 0.3)$ . We evaluate this claim using TNR: given a value of  $a_1$ , we analyze several candidate values of  $a_2$ , coarse-graining until the estimated value of  $c$  passes below a threshold, and then take a refined selection of  $a_2$ s around the value which had the greatest  $c$ . By using this method to seek a point at which  $c$  maintains an asymptotic value up to 12

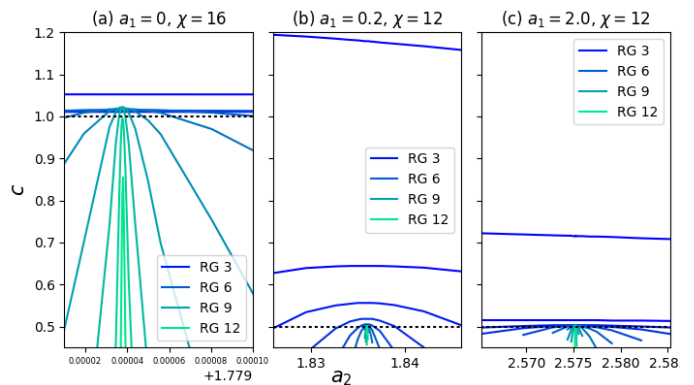


FIG. 7. Scanning in the neighborhood of the AKLT-Néel critical line, we find as we coarse-grain that the curve of estimated  $c$  versus  $a_2$  forms an increasingly narrow peak, with height  $c = 1$  at  $a_1 = 0$  and  $c = 1/2$  elsewhere.

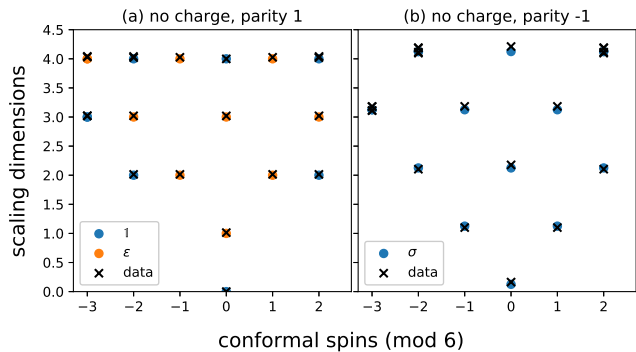


FIG. 8. The conformal tower at the critical line between the AKLT and Néel phases, specifically  $a_1 = 1.0$ ,  $a_2 = 2.575228$ , with  $\chi = 12$ ,  $\chi' = 10$ , after 7 RG steps. We find excellent replication of the conformal tower of the Ising CFT. Here we have marked theoretical values for the conformal towers of primary operators  $\mathbb{1}$ ,  $\epsilon$ , and  $\sigma$ . We find no scaling operators with nontrivial  $U(1)$  charge; what we find instead, with the spin operator  $\sigma$  in the parity -1 sector, is that (arbitrary)  $O(2)$  reflections play the role of spin-flips in the Ising model.

coarse-graining steps, we can resolve  $a_2$  to several parts per hundred thousand, as Fig. 7 demonstrates. Fig. 6 compares results from two values of the bond dimension and from the estimates in the original work. Moreover, this analysis neatly confirms the “Ising-like” nature of the transition; in Fig. 8, we see with TNR that the IR limit of the doubled vertex model along the transition exactly matches the Ising CFT with  $c = \frac{1}{2}$ , with spin-flips  $R_\phi^\pi$  playing the role of spin-flips in the Ising model. However in the  $a_1 \rightarrow 0$  limit we find  $c$  becomes 1, also demonstrated in Fig. 7.



$a_1$	$\chi = 12,$ $\chi' = 10$	$\chi = 16,$ $\chi' = 12$	$\chi = 20,$ $\chi' = 14$	$\chi = 24,$ $\chi' = 16$	NKZ
0.0	1.774789(6)	1.779038(1)	1.779243(1)	1.779348(1)	1.92(8)
0.1	1.795103(6)	1.798905(3)	—	—	1.93(8)
0.2	1.835964(6)	1.839119(6)	—	—	1.95(8)
0.3	1.892065(6)	1.894952(6)	—	—	1.99(8)

TABLE I. We use TNR to determine the critical line between the AKLT and Néel-ordered phases, increasing bond dimension from  $\chi = 12$  to  $\chi = 16$  at four points and then to  $\chi = 20$  and  $\chi = 24$  at one point to determine the accuracy of our estimates. Although we determine that the bias is much greater than the uncertainty of these estimates, we find that it appears nonetheless to be within  $\Delta a_2 < 0.01$  for our least accurate,  $\chi = 12$  estimates, and within  $\Delta a_2 < 0.001$  for our  $\chi = 16$  estimates. We also find that the error appears to decrease for increasing  $a_1$ , which also reduces the difference between the original Niggemann, Klümper, and Zittartz (NKZ) estimates and ours until they are within appropriate error of each other.

#### D. The XY-like phase

In a region near the origin  $a_1 = a_2 = 0$  of the phase diagram, we will find that the state has infinite correlation length (or equivalently, quasi-long-range order), as was reported for the analogous model on the honeycomb lattice.<sup>12</sup> This quasi-long-range-ordered region will explain much of the anomalous behavior observed in Fig. 5. In this phase, the doubled vertex model of (10) is described in the infrared limit by the continuously-parametrized field theory of the compactified free boson, much like the XY model in its low-temperature phase. We will begin by describing this conformal field theory (CFT), following Fendley<sup>33</sup> and Di Francesco, Mathieu, and Sénéchal<sup>34</sup>.

The compactified-free-boson CFT has central charge 1 and is characterized by a bosonic field  $\phi$  whose values are angles and which has some coupling constant  $g$ .<sup>35</sup> The field  $\phi$  itself is not a valid operator on the CFT due to its logarithmic divergences; however the theory admits derivative and vertex operators, represented in terms of the holomorphic and antiholomorphic components  $\phi = \varphi + \bar{\varphi}$  as

Field	$\Delta$	$s$
$\partial\varphi$	1	1
$\bar{\partial}\bar{\varphi}$	1	-1
$V_{e,m}$	$\frac{e^2}{2g} + \frac{m^2g}{2}$	$em$

(12)

where  $\Delta = h + \bar{h}$  is the scaling dimension and  $s = h - \bar{h}$  is the conformal spin,  $h$  and  $\bar{h}$  being the holomorphic and antiholomorphic conformal dimensions. The vertex operators  $V_{e,m} \propto :e^{i(e+gm)\varphi}e^{i(e-gm)\bar{\varphi}}:$  are indexed by an “electric charge”  $e \in \mathbb{Z}$  and “magnetic charge”  $m \in \mathbb{Z}$ . Here  $e$  is a  $U(1)$  charge, which is to say that a global rotation  $\phi \mapsto \phi + \phi_0$  will send  $V_{e,m} \mapsto e^{ie\phi_0}V_{e,m}$ ; magnetic charge indicates vortex winding number: in a configuration produced by inserting  $V_{e,m}(z)$ , there is a branch cut

from  $z$  to infinity (or to another vortex) around which  $\phi$  picks up  $2\pi m$ .

In the full global on-site  $O(2)$  symmetry of the compactified free boson or of the XY model, the charge- $\pm k$  representations  $v \mapsto e^{\pm ik\phi}v$  of the subgroup  $U(1) \subset O(2)$ , of rotations  $|s\rangle \mapsto e^{-i\phi S_z}|s\rangle$ , pair to form doublets; an additional pair of 1D representations have no  $U(1)$  charge but are either even or odd under reflections. Under this symmetry, the derivative operators belong to the rotation-invariant reflection-odd representation; the two electric operators  $V_{\pm e,0}$  for  $e \neq 0$  form a doublet; the four electromagnetic operators  $V_{\pm e,\pm m}$  for  $e, m \neq 0$  form a pair of doublets; and the magnetic operators  $V_{0,\pm m}$  for  $m > 0$  are exchanged under reflections, so that  $V_{0,m} + V_{0,-m}$  belongs to the trivial representation and  $V_{0,m} - V_{0,-m}$  belongs to the reflection-odd representation. In particular,  $V_{0,1} + V_{0,-1}$  has the smallest scaling dimension of any  $O(2)$ -invariant primary operator other than the identity, and will therefore induce a phase transition when it becomes relevant. As  $\Delta_{0,\pm 1} = \frac{g}{2}$ , and a scaling operator is relevant when  $\Delta < d$ , this occurs at coupling  $g = 2d = 4$ .

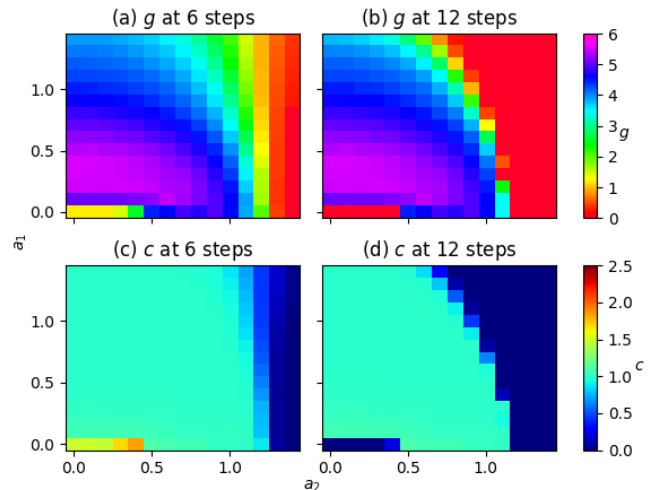


FIG. 9. Basic estimates of  $g$  and  $c$  from TNR,  $\chi = 20$ ,  $\chi' = 14$ . (a) After six coarse-graining steps we can see that the region  $g \geq 4$  is bounded by a curve which intersects the axes at roughly  $a_1 = 1.2$  and  $a_2 = 1.0$ . As  $a_2$  is held constant and  $a_1$  decreases,  $g$  increases to as much as 5.5 before falling off towards the  $a_2$  axis. (b) After 12 coarse-graining steps,  $g$  has remained approximately constant within the region where  $g \geq 4$ , but it has decreased, sometimes substantially, where  $g < 4$ . (c) After six RG steps  $c$  maintains a value very close to 1 in a region roughly corresponding to  $g > 2.5$ . (d) This is also true after 12 RG steps, but that region has shrunk due to changes in the estimated value of  $g$ . Between estimates for  $g$  and for  $c$ , we end up with an XY-like phase that's quite well-defined away from the pseudo-quasi-long-range ordered region.

We will conclude that this CFT describes the doubled

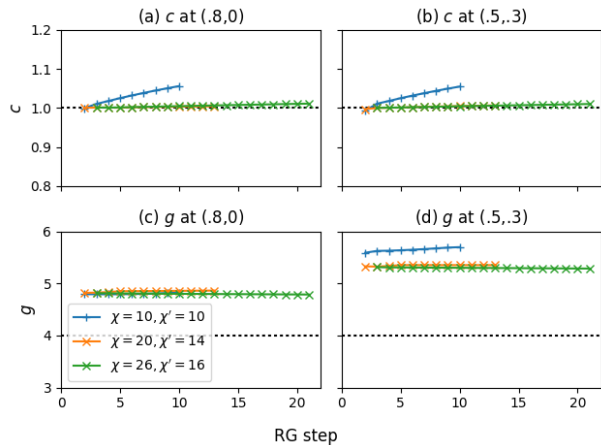


FIG. 10. Following the estimated quantities  $g$  and  $c$  with increasing system size - measured in number of coarse-graining steps - at different bond dimensions. (a),(b) For both  $a_1 = .8, a_2 = 0$  and  $a_1 = .5, a_2 = .3$ ,  $c$  converges as the bond dimension increases, and by  $\chi = 26$  maintains a value of  $1.005 \pm .005$  as coarse-graining increases the length scale. (c) At  $a_1 = .8, a_2 = 0$ ,  $g$  converges with increasing bond dimension, with a value of  $4.80 \pm .01$  at  $\chi = 26$  which is steady under coarse-graining. (d) At  $a_1 = .5, a_2 = .3$ ,  $g$  converges with increasing bond dimension, with a value of  $5.30 \pm .01$  at  $\chi = 26$  which is steady under coarse-graining. (Here, and in any other such presentations of data from TNR, we use + to mark data obtained while preserving  $\mathbb{Z}_2 \times \mathbb{Z}_2$  and  $\times$  to mark data obtained while preserving  $D_{2N}$ , typically  $D_{80}$ ; the latter is usually more consistent and demonstrates more stability.)

vertex model, including a transition at  $g = 4$ . By performing TNR (see Appendix A 3), we can approximate the value of the classical central charge  $c$  and the coupling  $g$  in much of the XY phase and estimate the contours of that phase. We find a region in which the estimated value of  $c$  converges to approximately 1 and the estimated value of  $g$  converges to varying values:  $g \simeq 4$  on the boundary of this region and increases to a value of about 5.5 going inward towards the origin. In Fig. 9 we use TNR with bond dimensions  $\chi = 20, \chi' = 14$  (which regulate the size of renormalized degrees of freedom in each half-step and intermediate step, respectively) to define this region: Its outer boundary intersects the  $a_1$  axis at approximately 1.2 and the  $a_2$  axis at approximately 1.1; its inner boundary is unclear. As will be discussed later, the results of this scan are not conclusive in the inner region, which requires analysis with higher bond dimensions.

Up to a certain point, however, the values from this analysis prove robust when we increase bond dimension, as shown for two values from the interior of the XY region in Fig. 10. Furthermore, in Appendix G, we analyze the conformal tower at these points in order to get a convincing confirmation that the doubled vertex model has as its infrared limit a compactified-free-boson CFT.

In Appendix B 2, we attempt to explain this using the spin-coherent-state picture as presented by Haldane<sup>16</sup>

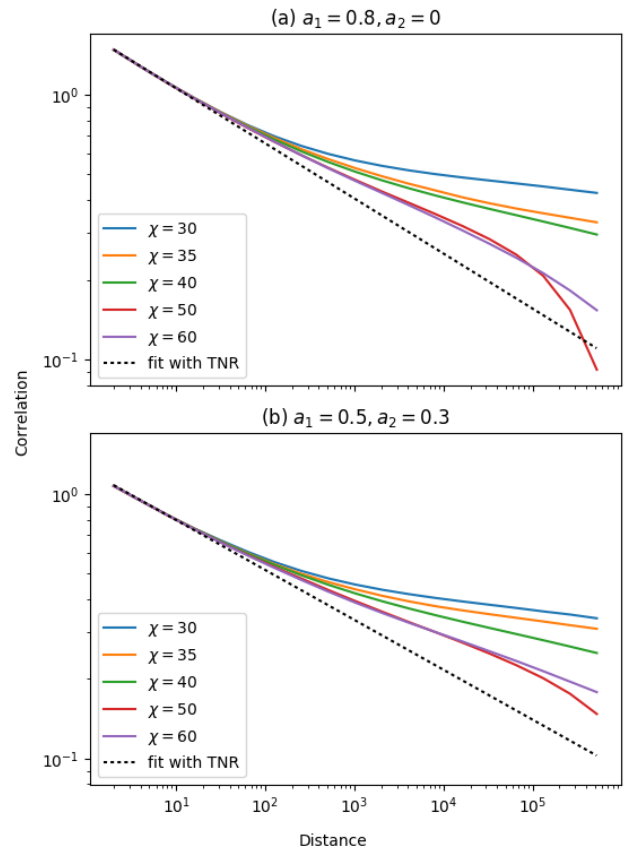


FIG. 11. Correlation functions of  $S_x$  from HOTRG, on a  $2^{21} \times 2^{21}$  torus, compared with power-law estimates of the form  $C(L) = C_0 L^{-\eta}$ , where  $\eta = 2\Delta = 1/g$  is determined by the TNR estimates in Fig. 10 and  $C_0$  is estimated to provide the best tangent line. In both cases we see the measured curve approaching the power-law estimate with increasing bond dimension. (a) At  $a_1 = .8, a_2 = 0$ , the TNR estimate gives  $\eta = 0.1887$ , and we estimate  $C_0 = 1.711$ . (b) At  $a_1 = .5, a_2 = .3$ , the TNR estimate gives  $\eta = 0.2083$ , and we estimate  $C_0 = 1.2309$ .

(see also Auerbach<sup>36</sup>). Within that framework,  $S_x$  and  $S_y$ , as classical observables in the sense of Fig. 3, should be proportional to the primary operators  $V_{1,0} \pm V_{-1,0}$ , which have scaling dimension  $\frac{1}{2g}$  and conformal spin 0 and which transform into each other under the  $k = 1$  irrep of the on-site  $O(2)$  symmetry. In particular, we expect the correlation-function behavior

$$\langle S_\phi(\vec{r}) S_\phi(\vec{r}') \rangle \sim |\vec{r} - \vec{r}'|^{2-d-\eta} = |\vec{r} - \vec{r}'|^{-\frac{1}{g}}, \quad (13)$$

where  $S_\phi$  is the combination  $S_x \cos \phi + S_y \sin \phi$ . As  $S_\phi$  is a quantum observable as well, if this power-law relation holds it implies quasi-long-range ordered behavior of the quantum model.

To this end we have attempted to extract the correlations of  $S_x$  at these points. Our current TNR methods cannot efficiently calculate correlation functions at the



bond dimensions of our probe, so we have instead used HOTRG; but this method cannot replicate long-range behavior of critical systems with finite bond dimension, so we instead try to replicate the  $\chi \rightarrow \infty$  limit by increasing the bond dimension. In Fig. 11 we demonstrate that the correlation functions thus obtained approach a curve  $C_0 r^{-\eta}$ , where  $\eta$  is the critical exponent expected from the previously-discussed TNR studies and the coefficient  $C_0$  is chosen to fit the HOTRG data. This demonstrates that the quasi-long-range order of the doubled vertex model does in fact reflect quasi-long-range order of the quantum state. In Appendix E, we additionally study the critical exponent  $\delta$ .

### E. The Kosterlitz-Thouless transition between the XY and AKLT phases

We have hypothesized that the XY phase is stable only when the long-range value of the coupling  $g$  is at least 4. Fig. 9 gives some evidence for this at selected length scales and fixed bond dimension. In Fig. 12, we take some points that we can predict to be near the phase transition and observe how estimates for  $c$  and  $g$  behave at very large length scales. The result confirms the expected behavior of  $c$  and  $g$  as asymptotic values. Moreover, a substantial increase in bond dimension from that used for Fig. 9 does not substantially alter the result, lending confidence to our conclusion. In Fig. 13 we apply loop-TNR and find results compatible with those obtained from Evenbly and Vidal’s TNR algorithm. In Appendix C we examine many points around the transition to try to see a more thorough picture.

We can also use correlation functions to confirm that points on either side of the supposed transition lie in, respectively, critical and non-critical phases. Contrasting Fig. 11 with corresponding data from outside of the transition as in Fig. 14, we find that in the latter case the correlation function converges to a form that exponentially decays to machine epsilon.

We see that, within what we label the XY phase, our estimates of  $g$  converge with successive coarse-graining operations, with small negative corrections that grow as we approach the transition, at which  $g$  converges to a value of approximately 4. Beyond the transition, the estimated  $g$  falls to zero, either starting below 4 and quickly dropping, or starting above 4, slowly declining until it passes below 4, and then quickly dropping, in both cases indicating that scale-invariance fails and so the doubled vertex model departs from the conformal invariance of the XY phase<sup>37</sup>. Either way, the estimate for  $c$  plateaus at approximately 1 and diverges noticeably from that value only when  $g$  is significantly less than 4 at the length scale in question. In fact, in Fig. 14 we will find that the length scale at which  $c$  measurably decays approximately predicts the correlation length.

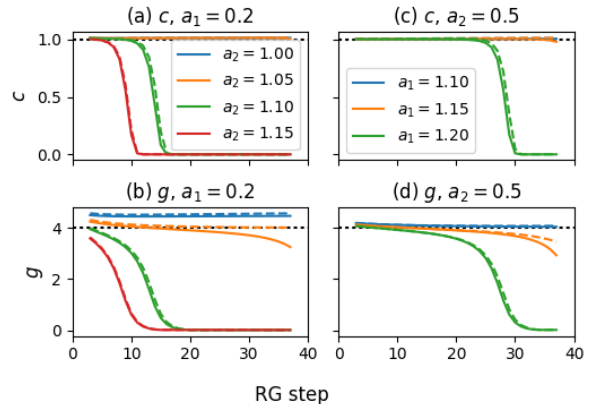


FIG. 12. We use TNR at  $\chi = 20$ ,  $\chi' = 14$  (dashed lines) and  $\chi = 30$ ,  $\chi' = 20$  (solid lines) to analyze the long-range behavior of the system in the immediate vicinity of the KT-like transition at  $a_1 = 0.2$  (a),(b) and  $a_2 = 0.5$  (c),(d). We examine values of our estimates for the classical central charge  $c$  (a),(c) and the coupling  $g$  (b),(d) after successive coarse-graining steps, and conclude: (i) While corrections to behavior from increasing bond dimension are present, they are unlikely to influence estimates of the location of the transition by more than about  $|\Delta \vec{a}| \simeq 0.05$ , which indicates that the  $\chi = 20$  behavior of Fig. 9 is largely accurate. (ii) The idea that a coupling  $g < 4$  induces the appearance of a length scale is readily confirmed; in fact in (b) we see that, at  $a_1 = 0.2$ ,  $a_2 = 1.05$ , the system appears to flow to a non-trivial fixed point when  $g$  barely fails to cross below 4 at  $\chi = 20$ , but at  $\chi = 30$  a small correction to shorter-ranged values of  $g$  induces this crossing and causes a violation of scale invariance. Moreover,  $c$  only deviates noticeably from 1 at length scales where  $g$  is rapidly flowing towards 0, but invariably does so under those conditions. (iii) In (b) we see much more substantial corrections to  $g$  at shorter length scales than in (d), likely related to the much stronger persistence of pseudo-quasi-long-range behavior near the points analyzed in (d) than (b) - specifically, the same perturbations which we expect to induce the transition for  $g < 4$  may also lead to corrections to the coupling for  $g > 4$ , such that the suppression of these perturbations that increases the persistence of pseudo-quasi-long-range order near the  $a_1$  axis may also reduce corrections to  $g$  near the transition in that region.

### F. The pseudo-quasi-long-range ordered region

Informed by the observation that the decay of  $c$  roughly predicts correlation length, we note that we can generally estimate  $c$  to be about 1 much further into the AKLT phase for small  $a_2$  than it does for small  $a_1$ ; in particular this behavior is most evident in Figs. 9 and 25. This suggests an extended region of “pseudo-quasi-long-range order” (behavior which imitates that of the quasi-long-range ordered XY phase up to length scales large enough that they may be experimentally impractical) near the  $a_1$  axis. In fact in Fig. 1, we delineate a region “above” the XY phase that is nearly as large, which we believe to have correlation length of about 1000 times the lattice

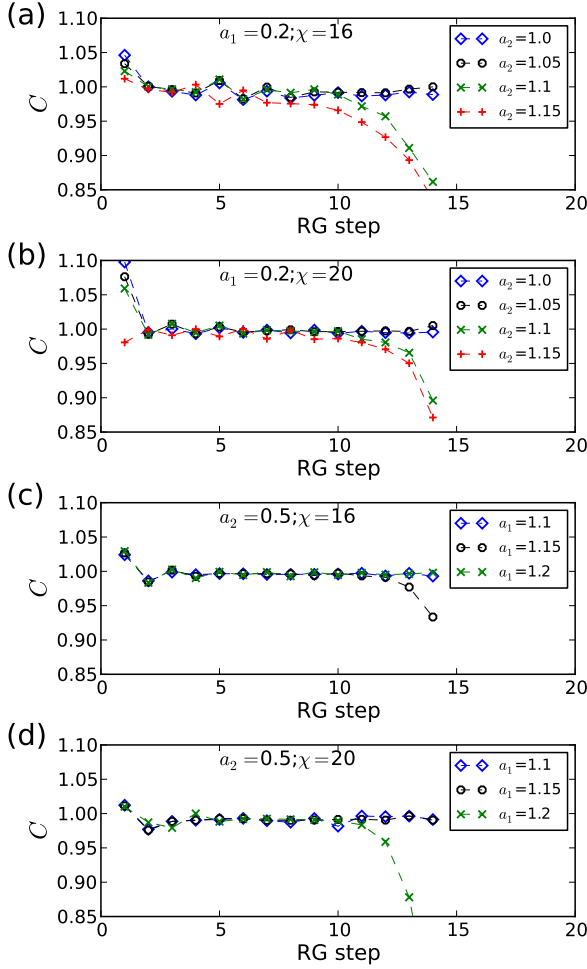


FIG. 13. We use loop-TNR to analyze the same points in the phase diagram as in Fig. 12, estimating  $c$  for  $\chi = 16$  and  $\chi = 20$ . Although the results are noisier than those obtained with TNR (possibly partly since we did not preserve symmetries when using loop-TNR). By  $\chi = 20$  the results are largely similar to the TNR results: when we consider the KT transition at  $a_1 = 0.2$ , we observe that  $c$  appears stable for  $a_2 = 1$  and  $a_2 = 1.05$  but not  $a_2 = 1.1$  or  $a_2 = 1.15$ ; meanwhile, when we consider the KT transition at  $a_2 = 0.5$ , we observe that  $c$  appears stable for  $a_1 = 1.1$  and  $a_1 = 1.15$  but not for  $a_1 = 1.2$ .

spacing or more. (Such behavior has, notably, interfered with attempts to delineate the XY phase using methods other than TNR, even at relatively high bond dimensions.) Based on the analysis of Haldane<sup>16</sup>, we believe this is because the system in this region resembles a spin-1 antiferromagnet well enough that tunneling processes of odd winding number, including those that induce the KT transition, are almost suppressed and can therefore only weakly break scale invariance. We present this argument in somewhat more detail in Appendix B 4.

We may also confirm the KT transition using the physical critical exponent  $\delta$ , as in Appendix E, or use the

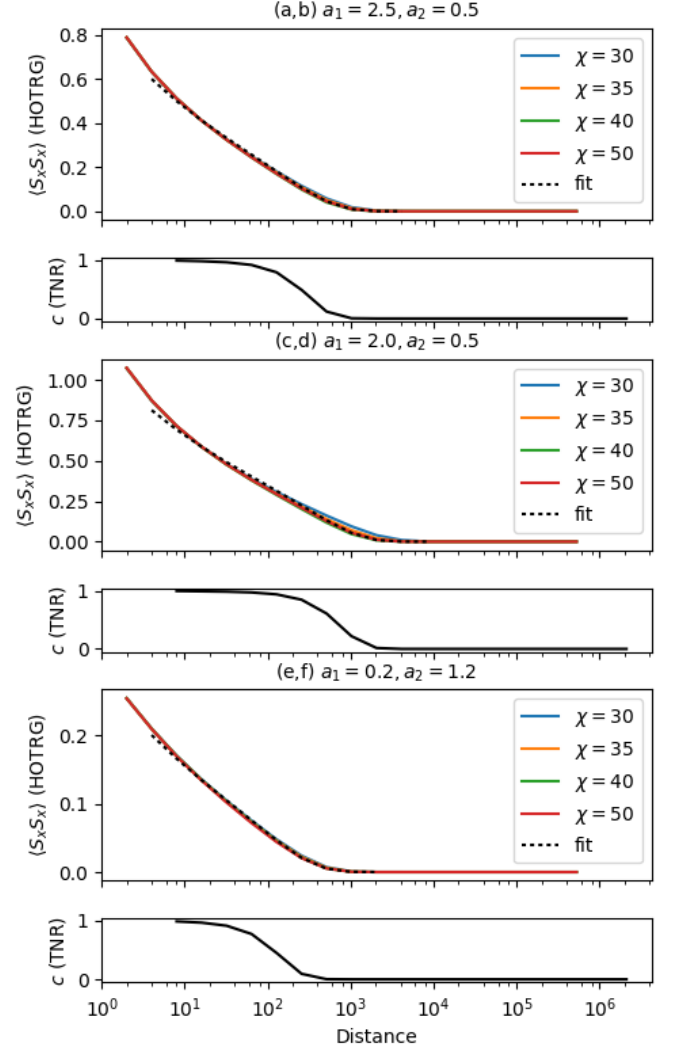


FIG. 14. Using HOTRG, we examine the correlation function  $\langle S_x S_x \rangle$  at several points inside the AKLT phase, varying bond dimension to confirm convergence and fitting the highest-bond-dimension curves to the exponential-decay form  $C(r) = C_0 r^{-\eta} e^{-r/\xi}$ . Additionally, by interpolating from TNR data with  $\chi = 20$ ,  $\chi' = 14$ , we estimate the classical central charge at the length scale of the correlation length  $\xi$  determined by fitting and find that the sharp falloff in estimated  $c$  roughly predicts the correlation length, with  $c(\xi) \sim 0.35$ . (Note that, as we obtain  $c$  by comparing transfer matrices  $M$  of different length, our estimates of  $c$  do not correspond to a precise length; here we use  $c(L)$  to refer to the  $c$  obtained by comparing  $M(3L)$  and  $M(2L)$ .) (a),(b) At  $a_1 = 2.5, a_2 = 0.5$ , toward the outside of the pseudo-quasi-long-range ordered region, we obtain  $C_0 \simeq 0.853$ ,  $\eta \simeq 0.247$ , and  $\xi \simeq 365$ , with  $c(\xi) \simeq 0.30$ . (c),(d) At  $a_1 = 2.0, a_2 = 0.5$ , deeper within the pseudo-quasi-long-range ordered region, we obtain  $C_0 \simeq 1.113$ ,  $\eta \simeq 0.223$ , and  $\xi \simeq 693$ , with  $c(\xi) \simeq 0.44$ . (e),(f) At  $a_1 = 1.2, a_2 = 0.2$ , near the  $a_2$  axis and thus further from pseudo-quasi-long-range ordered effects, we obtain  $C_0 \simeq 0.287$ ,  $\eta \simeq 0.245$ , and  $\xi \simeq 203$ , with  $c(\xi) \simeq 0.21$ .

corner entropy to approximate the boundary of the XY phase, as in Appendix F. The results are consistent with those from TNR, although not as precise.

### G. The elusive product-state phase

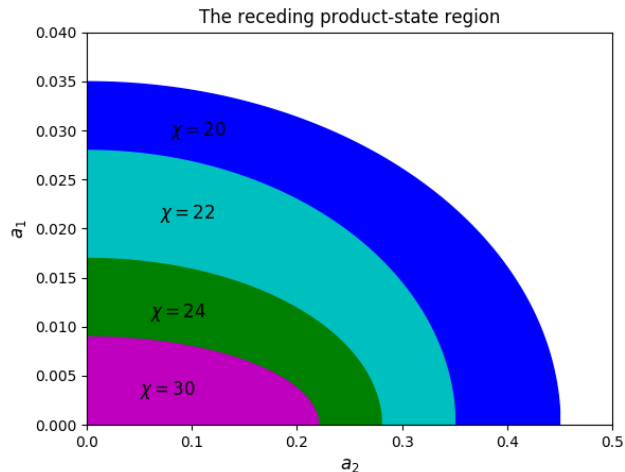


FIG. 15. A very rough estimate of the bounds of the product-state region obtained using TNR at various bond dimensions. For a given bond dimension  $\chi$ , points within the regions labeled with  $\chi$  or  $\chi_2 > \chi$  are expected to correspond to parameters for which TNR will report trivial behavior at that bond dimension; outside of that region XY-like behavior is expected at that bond dimension. Most of the data used to establish these boundaries can be found in Figs. 17 and 26.

When  $a_1 = a_2 = 0$ , however, the deformation projects the state onto the product  $|0, 0, \dots, 0, 0\rangle$ . Naïvely, we expect to find a gapped, entirely trivial phase in a region around this. But the amplitude of  $|0, 0, \dots, 0, 0\rangle$  in the AKLT state is precisely equal to the partition function of a six-vertex model (specifically at the “square-ice” point  $a = b = c = 1$ ), whose degrees of freedom are reflected in the virtual, or entanglement, degrees of freedom of the PEPS representation of this state. On the square lattice this model has been well-studied and is known to be critical, behaving in the infrared as the compactified free boson CFT with coupling  $g = \frac{1}{3}$ . At this point, therefore, the doubled vertex model is critical with  $c = 2$  despite the quantum state being trivial in every way.

In TNR studies of the region of the phase diagram surrounding this point, when we approach the origin *with fixed bond dimension* we find that the system appears to encounter a second KT-like transition, visible in Fig. 9:  $g$  appears to fall from a maximum value, ultimately reaching a value of 4 after which the behavior ceases to be critical, with  $c$  ultimately falling to 0 rather than remaining stable. This behavior is shown in more detail in Appendix C. We may also observe such behavior by analyzing simulated  $S$  and  $T$  traces as in Fig. 16, which

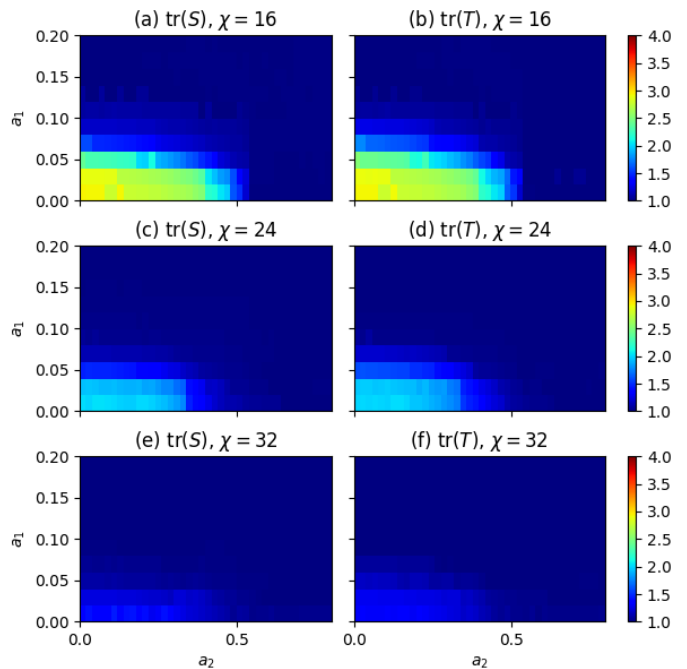


FIG. 16. Traces of the simulated modular  $S$  and  $T$  matrices obtained by inserting virtual symmetry matrices  $\sigma_z$ , using HOTRG with bond dimensions (a),(b)  $\chi = 16$  (c),(d)  $\chi = 24$  (e),(f)  $\chi = 32$ . We see that both traces appear to be close to 1 in much of the XY phase, but rise toward the trivial value of 4 in a small region within  $a_1 < .04$ ,  $a_2 < .4$ , similar to the estimates in Fig. 26. However, as the bond dimension grows, the extent of this region appears to shrink, much as in Fig. 15.

appear to reach a trivial value of 4 in this region.

However, when we increase the bond dimension, we find that the boundary of this transition recedes towards the origin as in Fig. 15, and points which appear to have finite correlation length at lower bond dimension tend to obtain a central charge of 1 at higher bond dimensions. In Appendix D we analyze individual points near the origin of the phase diagram and find that results are highly sensitive to bond dimension. In fact, when we increase the bond dimension from  $\chi = 30$ ,  $\chi' = 20$  to  $\chi = 36$ ,  $\chi' = 24$ , rather than straightforward behavior in a well-defined region we find noisy fluctuations in  $g$  (some of which do pass below 4), as in Fig. 17. Some results from  $\chi = 42$ ,  $\chi' = 28$  are also presented in Appendix D; they do little to clarify this picture.

The principal alternatives we should consider are that:

1. The product-state phase has finite, but small, extent and is defined by a KT-like transition much as the data in Fig. 9 suggests;
2. The product-state phase does not exist; rather, the coupling  $g$ 
  - (a) peaks along some curve, before falling to a limiting value, likely 4, approaching the origin;

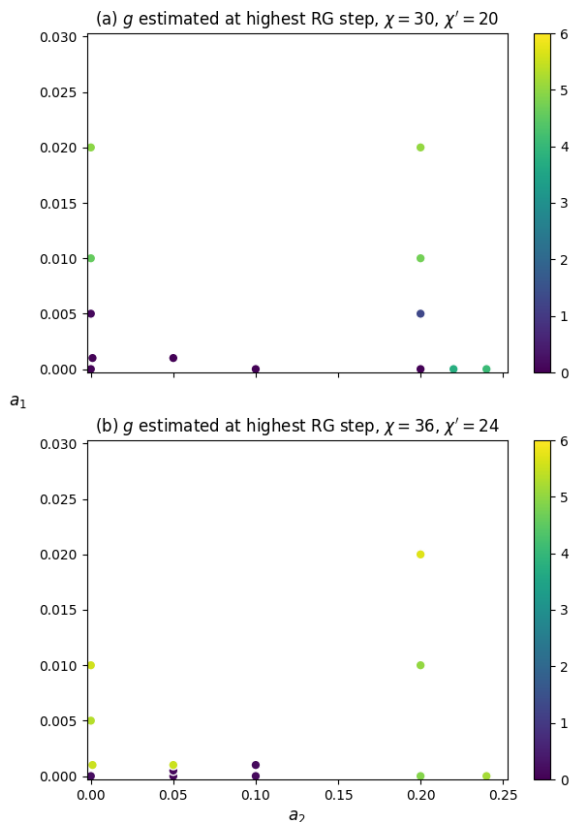


FIG. 17. We perform 12 coarse-graining steps of TNR at several points near the origin, estimating  $g$  after the final coarse-graining step and using that to determine the behavior in this region. (a) For  $\chi = 30, \chi' = 20$ ,  $g$  consistently falls as we approach the origin within the area shown, inducing a KT-like transition into an apparent trivial phase in a region which intersects the  $a_1$  axis at  $a_1 \simeq 0.01$  and the  $a_2$  axis at  $a_2 \simeq 0.2$ . (b) For  $\chi = 36, \chi' = 24$ , however, there does not appear to be a well-defined product-state phase, at least for  $a_1 \geq 0.001$ . Rather, we observe fluctuations in the estimated value of  $g$  with no discernable pattern and with non-trivial limiting values of  $g$  found as close to the origin as  $(a_1, a_2) = (0.001, 0.001)$ .

- (b) keeps rising to a limiting value of 6 or greater approaching the origin; or
- (c) keeps rising to  $\infty$ , much as at the ferromagnetic Heisenberg point of the XXZ model.<sup>33</sup>

It is currently unclear which of these is most likely, but evidence does suggest the absence of a separate gapped and completely trivial phase.

To this lack of evidence we add that the arguments we have used to justify our expectation of a trivial phase are inherently flawed. The parent Hamiltonian<sup>10</sup> derived by Niggemann, Klümper, and Zittartz does not extend to

the limiting case  $a_1 = a_2 = 0$ , nor does the formulation in (6): in order to project out spin values, a parent Hamiltonian will generally have to increase its rank, which is impossible to do via continuous deformation. For example, at all points in the interior of the phase diagram, the two-site parent Hamiltonian will annihilate  $|12\rangle - |21\rangle$  (see Eq. 11 of Niggemann, Klümper, and Zittartz<sup>10</sup>); therefore, so must the limit of any sequence of such Hamiltonians. For  $a_1 \rightarrow 0$  or  $a_2 \rightarrow 0$ , this introduces the possibility that some sites may have (respectively)  $S_z = 1$  or  $S_z = 2$  with nonzero probability in the ground space of the limiting Hamiltonian, even though they have been projected out of the deformed state.

We also note that, if we were to include the product state at  $a_1 = a_2 = 0$  in the phase diagram, we would be implicitly suggesting that nearby states in the phase diagram could be obtained by perturbing this product state, which should in turn imply that it is enclosed in the phase diagram by a phase of finite correlation length. However, we suggest that such “perturbations” may instead have quasi-long-range correlations and therefore should, in the thermodynamic limit, dominate the original (product) state at any magnitude. We conclude, therefore, that if we wish to connect the point  $a_1 = a_2 = 0$  with the surrounding points of the phase diagram, we should do so with extreme caution.

#### IV. RE-EXAMINING THE XY PHASE ON THE HONEYCOMB LATTICE

In Huang, Wagner and Wei<sup>12</sup>, the analogous model for the honeycomb lattice was examined using tensor-network methods, and it was concluded that a quasi-long-range ordered phase exists close to the value  $a = 0$  of the perturbation parameter. Having refined our analysis to more sensitively judge the properties and boundaries of such a phase, as in Sec. IIID, we return to this model. The numerical methods are the same as for the square-lattice model (save for a correction in order to account for the anisotropy induced by blocking honeycomb-lattice sites into square-lattice sites).

In Fig. 18, we observe that successive applications of TNR coarse-graining, with increasing bond dimension, fail to maintain evidence of a “transition” to a quasi-long-range ordered region; rather, we observe that what appears to be an XY phase shrinks in size as RG proceeds. We nowhere and at no scale estimate  $g \geq 4$ , and what was previously believed to be a phase with quasi-long-range order appears to give way to a region with pseudo-quasi-long-range order similar to the analogous region of the AKLT phase on the square lattice. Much as we claim that, when  $a_2 \sim 0$ , the square-lattice state approximates a spin-1 antiferromagnet in which isolated vortices of winding number 1 (modulo 2) are suppressed by square-lattice symmetries, we claim that, when  $a \sim 0$ , the honeycomb-lattice state approximates a spin- $\frac{1}{2}$  antiferromagnet in which isolated vortices of winding num-

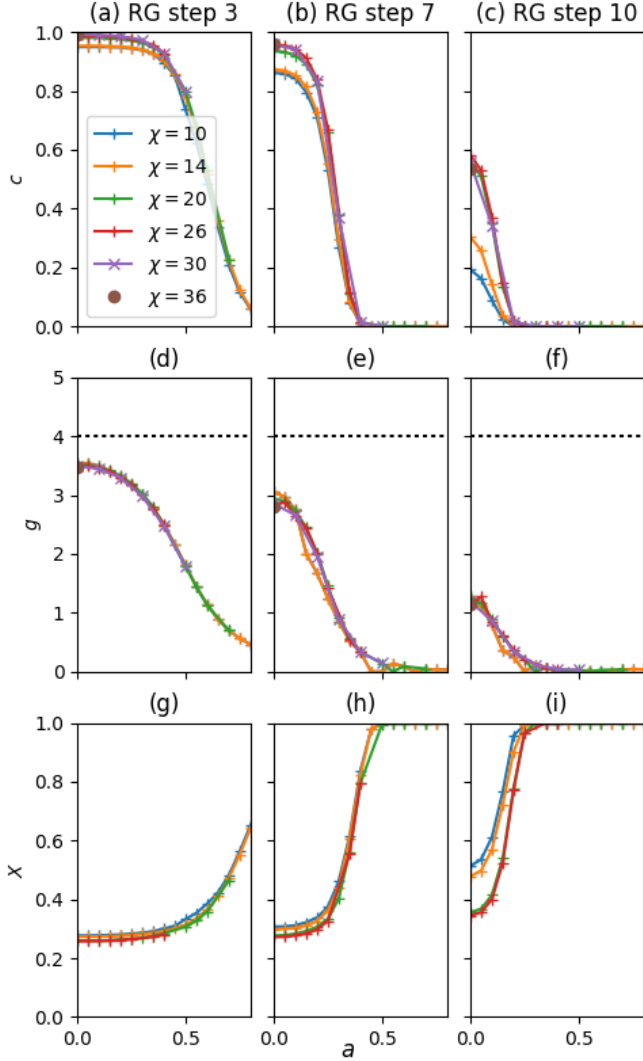


FIG. 18. We use TNR at various bond dimensions to analyze the honeycomb-lattice system. (a) At linear system size  $O(10)$ , a region extending to  $a \simeq 0.4$  appears to have long-range behavior with  $c = 1$ . (b) For system length  $O(100)$ , this has shrunk to within  $a \simeq 0.1$ . (c) By system length  $O(1000)$ , all points clearly do not exhibit quasi-long-range ordered behavior. (d) The value of  $g$  estimated at small system sizes is close to 3.5 at  $a = 0$ , and smoothly falls off leaving the “pseudo-quasi-long-range ordered” region. (e),(f) At all points the estimate of  $g$  gradually falls off to 0. (g),(h),(i) TNR estimates of the Chen-Gu-Wen  $X$ -ratio<sup>38</sup> rise towards the AKLT-phase value of 1. Within the pseudo-quasi-long-range ordered region, however, they may appear to take a different, nontrivial intermediate value up to fairly large length scales.

ber 1 and 2 (modulo 3) are suppressed by honeycomb-lattice symmetries. If this is true, we expect that XY couplings as low as  $g = \frac{4}{9}$  should become “approximately stable,” reproducing pseudo-quasi-long-range ordered behavior. In Fig. 19, we see that even at the point  $a = 0$ , as we increase the bond dimension we consistently ob-

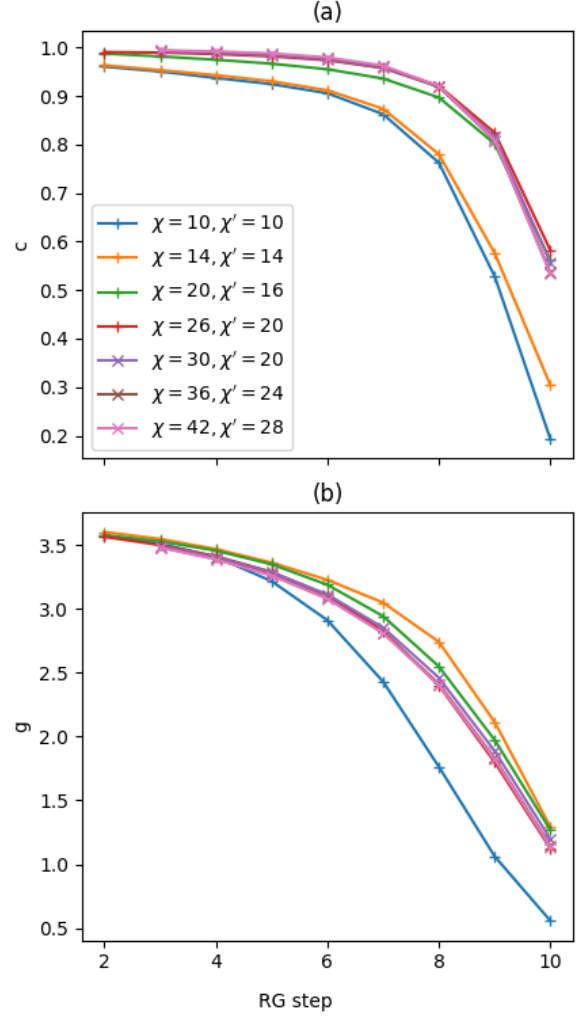


FIG. 19. We use TNR to analyze the honeycomb system at  $a = 0$ , the most likely candidate for critical behavior. (a) Although increasing bond dimension tends to raise the estimated value of the classical central charge  $c$  towards 1, as a function of the length scale  $c$  appears to converge to a decaying form at the highest bond dimensions tested. (b) When we estimate the coupling  $g$ , we find that its initial value always appears to be close to  $3.6 < 4.0$ , and that it never appears to be stable under coarse-graining. We additionally note that several successive increases in bond dimension, from  $\chi = 26, \chi' = 20$  to ultimately  $\chi = 42, \chi' = 28$ , do not substantially affect the estimates for either  $c$  or  $g$ .

serve behavior consistent with finite, but large, correlation length.

## V. DISCUSSION

We have used tensor-network methods to explore the two-parameter phase diagram of the deformed-AKLT model on the square lattice. In addition to confirming our



expectations about the AKLT and Néel phases, we find a well-defined quasi-long-range ordered phase with properties resembling those of the classical XY model, including a Kosterlitz-Thouless (KT)-like transition. Evenbly and Vidal’s TNR algorithm<sup>32</sup> gives us a way to effectively and accurately extract a substantial amount of information about this behavior; prior to its development, we may not have even been able to conclusively demonstrate the phase’s existence, as was the case when tensor-network methods were previously applied to a similar question.<sup>12</sup> Although we have *not* been able to efficiently use TNR to directly compute correlation functions, it has yielded predictions about critical exponents  $\eta$  and  $\delta$  that we have been able to roughly confirm with HOTRG. We also find from our analysis that a “pseudo-quasi-long-range ordered” region of persistently large correlation length extends from part of that transition. We explain this by arguing that isolated tunneling processes are approximately suppressed, a claim which could benefit from more rigorous analysis.

We have also re-examined the honeycomb case. Using the analysis that we have applied to the XY phase of the square-lattice model, we have found that the region previously identified as an XY phase is instead a pseudo-quasi-long-range ordered region of the AKLT phase; that model has no true XY phase.

We also find some peculiar behavior when the parameter  $a_1$  is very small. Aside from an apparent crossover in the AKLT/Néel transition in this limit, we find that there is a region close to the origin ( $a_2 < 0.3$ ,  $a_1 \ll 0.1$ ) where the system’s behavior is no longer evident. Although we have largely exhausted our resources in attempting to determine the exact behavior in that region using current methods, we may be able to extract more information either by refining our techniques, for example by taking further advantage of the symmetry<sup>24</sup>, or by analyzing the  $a_1 = 0$  line specifically with approaches that may only apply there. In doing so we would wish to determine whether or not this region contains a distinct phase with no long-range order, if so, what the nature of the transition is, and if not, what the system’s behavior is as  $a_1$  and  $a_2$  are both reduced to 0.

Future work may examine the mechanism of the Kosterlitz-Thouless transition, including the origin of the coupling which we have labeled  $g$  and the role of tunneling processes. Extensions to this system, such as deformations of spin- $2m$  AKLT states, a spin-1 AKLT-like state, or the kagome-lattice AKLT state, may also give us more information about the underlying physics. The state’s behavior along the  $a_1 = 0$  axis, and how it relates to the behavior in the interior of the phase diagram as  $a_1 \rightarrow 0$ , may have much to tell us about the behavior of the XY phase near or in the “product-state” region.

## ACKNOWLEDGMENTS

The authors would like to acknowledge useful discussions with Alexander Abanov, Ian Affleck, and especially Cenke Xu, who suggested the physical picture for the pseudo-quasi-long-range ordered region. This work was partially supported by the National Science Foundation under Grant No. PHY 1620252 and Grant No. PHY 1314748.

### Appendix A: Review of numerical methods

In this work, we employ several numerical tensor-network methods; here, we briefly discuss each of them. We use different methods for their varying strengths: that is, which quantities we can use them to (efficiently) calculate, and which regimes they are accurate in.

#### 1. The corner transfer matrix method

We first describe the corner transfer matrix renormalization group (CTMRG), which was first introduced by Baxter.<sup>40</sup> It was further developed and applied as a numerical method for analyzing classical statistical systems by Nishino and Okunishi.<sup>27</sup> More recently, it was adapted to the contraction of tensor networks by Orus.<sup>28</sup>

CTMRG represents a classical partition function, or equivalently the norm of a quantum state as in (10), using a tensor environment  $\{C_1, C_2, C_3, C_4, T_1, T_2, T_3, T_4\}$ , where the  $C_i$  represent quadrants of the plane and the  $T_i$  represent rays extending from the “central” site whose environment we are considering, as in Fig. 20. To obtain these environment tensors, we initialize them randomly, and then iteratively add rows and columns of sites, which we add to the environment tensors, truncating pairs of bonds to prevent exponential growth of the bond dimen-

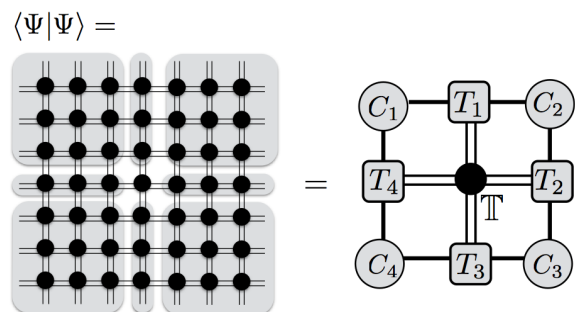


FIG. 20. In CTMRG, we represent each quadrant of the plane, as well as rays extending from a given site, as individual tensors. Typically we represent the entire norm squared through a contraction of the four quadrant tensors, four ray tensors, and one double tensor representing a single site. Additional rows and columns can be inserted as needed.



sion. Once the environment tensors have been determined, we can evaluate the partition function and the expectation values of local observables of a classical statistical system, or the norm and the expectation values of a quantum state represented by a tensor network state, as the entire network eventually reduces to only a few sites, on which we can directly calculate the necessary tensor trace.

In addition to computing expectation values, we can use CTMRG to directly calculate correlation length, as follows. We may insert columns of sites (or, more precisely, contracted  $\{T_1, \mathbb{T}, T_3\}$  triples) to “lengthen” the system and obtain correlation functions of large (horizontal) distances; when we do the contracted network begins to resemble the partition function of a one-dimensional statistical system, the columns  $M = \text{tTr}(T_1 \mathbb{T} T_3)$  being transfer matrices. We note that convergence of the environment tensors suggests that the columns at either end approximate the dominant left and right eigenvectors of these transfer matrices. If  $\lambda_i$  are the eigenvalues ordered by magnitude, this means that for some operator  $\mathcal{O}$  with  $\text{tTr}(T_1 \mathcal{O} A^* T_3) = M_{\mathcal{O}}$ , similar to the correspondence in Fig. 3,

$$\begin{aligned} \langle \mathcal{O}(0) \mathcal{O}(L) \rangle &= \frac{v_L M_{\mathcal{O}} M^{L-1} M_{\mathcal{O}} v_R}{v_L M^{L+1} v_R} \\ &= C_0 + C_1 \left( \frac{\lambda_1}{\lambda_0} \right)^L + O((\lambda_2/\lambda_0)^L), \quad (\text{A1}) \end{aligned}$$

where constants  $C_0$  and  $C_1$  can be easily determined from  $M_{\mathcal{O}}$  and the eigenvalues and eigenvectors of  $M$ . Thus the correlation function decays exponentially with decay constant  $\log(\lambda_0/\lambda_1)$ .

We may also use CTMRG to extract a quantity which we refer to as the “corner entropy”. We may imagine a classical partition function as representing a Euclidean path integral of a 1D quantum system<sup>41</sup>, with the upper and lower half-planes representing the ket and bra vectors, respectively. In this case, once we have completed the CTMRG procedure and represented the partition function as the contraction  $\text{tTr}(C_1 C_2 C_3 C_4)$ , we should expect that the bond between  $C_1$  and  $C_4$  should approximate the “physical” state of the entire left half of the line and the bond between  $C_2$  and  $C_3$  should likewise approximate the “physical” state of the right half of the line. Then we expect the tensor trace of these four tensors with the bond between  $C_1$  and  $C_4$  left open to approximate the (non-normalized) reduced density matrix of the left half of the system - that is, its spectrum should resemble a truncated version of the actual reduced density matrix. Then the entropy of the spectrum of the open tensor trace  $\rho_{\text{corner}} = \text{tr}(C_1 C_2 C_3 C_4)$  should approximate the entanglement entropy between the left and right rays. We thus call the quantity  $S_{\text{corner}} = -\text{tr}(\rho_{\text{corner}} \log \rho_{\text{corner}})$  the “corner entropy.”

In a technique closely related to CTMRG, which we refer to as the quantum-state corner transfer matrix method or quantum-state renormalization group

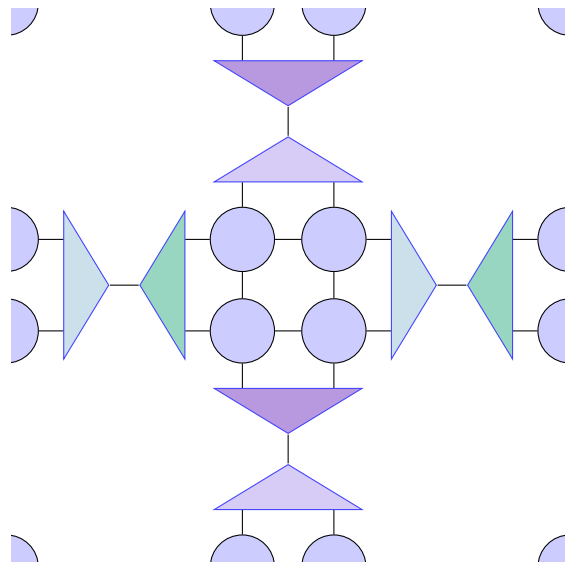


FIG. 21. Spin-blocking with HOTRG, wherein projective truncations are used to reduce pairs of vertical bonds, and then pairs of horizontal bonds, into single bonds of comparable bond dimension. Four sites are then turned into a single site, with the interior bond of the projective truncation used as the new bond of the coarse-grained “site”.

(QSRG), we may use the tensor environment to represent the quantum state rather than the norm-squared.<sup>42</sup> Each environment tensor has a “physical” index which represents the physical content of the state in the respective region of the lattice and which is renormalized along with the virtual bonds as rows and columns of sites are added. This method can be useful for approximating entanglement spectra.

## 2. Higher-order TRG

The remaining methods we will describe are coarse-graining methods, implementations of real-space renormalization inspired by Kadanoff’s spin-blocking method. In these methods, we combine blocks of site tensors into a single unit and apply some method to discard (hopefully irrelevant) information so that the bond space of the blocked tensor remains manageable. The resulting tensor represents a site of a coarse-grained lattice. In this way, we “renormalize” an  $N \times N$  partition function into an  $N/2 \times N/2$  partition function and repeat until the partition function can be directly evaluated. We typically think of this as an implementation of the renormalization group in which the couplings manifest as tensor elements.

The simplest of the methods that we will use is Xie et al.’s higher-order tensor renormalization group<sup>43</sup> (HOTRG). The fundamental idea is projective truncation: We take a pair of bonds, each contracted between two different tensors, and insert an orthogonal projector

$$\mathbb{P}^{ij}_{i'j'} = W^{ij}_k W^\dagger_{i'j'}{}^k, \quad (\text{A2})$$

where the tensor  $W$  is an isometry between the product of the vector spaces denoted by indices  $i$  and  $j$ , and the vector space denoted by index  $k$  which will represent renormalized degrees of freedom. The isometries are typically determined iteratively, using the principle that given an environment matrix  $E$ , when seeking a unitary matrix  $W$ , the contraction  $\text{Tr}(EW)$  is minimized by  $W = U^\dagger V$ , where  $E = UDV^\dagger$  is the singular value decomposition of  $E$ . Once the unitaries have been determined, they are typically then contracted with other tensors in such a way that the new virtual index  $k$  becomes a bond index.

In HOTRG, we use projective truncation to coarse-grain bonds by pairing them together - first vertically, then horizontally. This means that an  $N \times M$ -site lattice becomes an  $N \times M/2$ -site lattice, and then a  $N/2 \times M/2$ -site lattice. The way that bonds are collected to accomplish this is demonstrated in Fig. 21.

HOTRG provides a straightforward method for consolidating the information that is “located” at adjacent sites or edges, and as such allows for a relatively controlled computational cost in calculating expectation values and correlation functions. This also provides a way to renormalize string defects expressed as matrix product operators, such as those used to calculate modular  $S$  and  $T$  matrices in topological models<sup>25</sup> or simulated modular  $S$  and  $T$  matrices in SPT models<sup>13</sup>, by collecting defect tensors that lie along adjacent bonds and coarse-graining them along with the bonds.

### 3. Tensor Network Renormalization

CTMRG and coarse-graining methods like HOTRG, while highly effective in many situations, typically cannot effectively analyze systems with high correlation length. In order to extract information about systems that do have high correlation length, which is to say primarily those that exhibit or approximate critical behavior, we must use more complex techniques, primarily the method of tensor network renormalization (TNR) introduced by Evenbly and Vidal.<sup>32,41,44–46</sup> The algorithm is based on Vidal’s concept of entanglement renormalization, and we will only be able to represent it in the heuristic terms presented in Fig. 22.

While it is possible to use TNR to extract physical data such as expectation values, the methods to do so are typically quite computationally expensive, prohibitively so at the bond dimensions we have been primarily using. Instead we focus on the method<sup>45</sup> of using Cardy’s formula for the partition function on a torus in terms of conformal data<sup>47</sup>, in which we diagonalize an  $n$ -site transfer matrix with a one-site rotational twist and find that its eigenvalues are

$$\lambda_\alpha \simeq e^{-\frac{2\pi}{n}(\Delta_\alpha - \frac{c}{12}) + nf + \frac{2\pi i}{n}s_\alpha}, \quad (\text{A3})$$

where  $\alpha$  indexes scaling operators with scaling dimension  $\Delta_\alpha$  and conformal spin  $s_\alpha$ ,  $c$  is the central charge,  $f$  is a nonuniversal free-energy constant, and equality

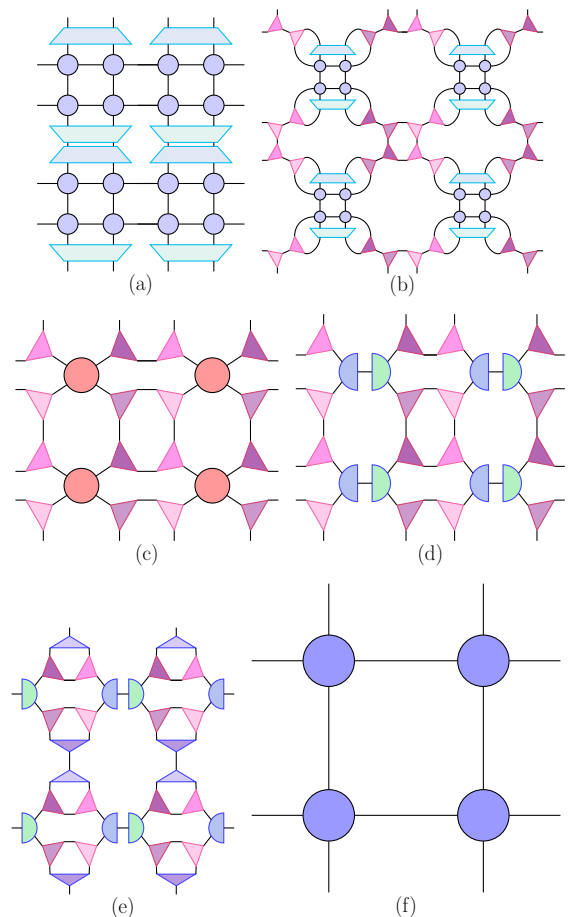


FIG. 22. The TNR procedure:<sup>44</sup> (a) Disentangler pairs  $u^\dagger u$  are added across pairs of vertical bonds. As the disentanglers are unitary, this is a resolution of the identity. (b) Projective truncations  $v_L^\dagger v_L$  and  $v_R^\dagger v_R$ , which have intermediate bond dimension  $\chi'$ , approximate the identity on nearby pairs of vertical and horizontal bonds at the corners of blocks of sites.  $v_L$ ,  $v_R$ , and  $u$  are iteratively optimized to maximize how well we approximate  $2 \times 2$  site blocks with the corresponding objects. (c) The sub-networks consisting of  $2 \times 2$  blocks of site tensors and the disentanglers and isometries that share bonds are contracted to yield intermediate tensors. (d) These intermediate tensors are split using a truncated singular value decomposition, wherein the truncation signifies eliminating all but  $\chi$  of the  $\chi'^2$  singular values so that the dimension of the new bond is  $\chi$ . (e) A projective truncation  $w^\dagger w$  with intermediate bond dimension  $\chi$  is placed across pairs of vertical bonds. (f) The collection of eight tensors whose boundary is the virtual bonds of dimension  $\chi$  formed in the last two steps is contracted to yield the site tensor at the next level of renormalization.

only holds as irrelevant perturbations vanish: that is, as coarse-graining takes us towards the thermodynamic limit. Note that we must analyze the transfer matrix at multiple sizes to isolate  $c$  and  $f$ ; that adding sites to the transfer matrix increases both the number of eigenvalues for which we may expect this approximation to be valid and the range of conformal spins which it distinguishes;

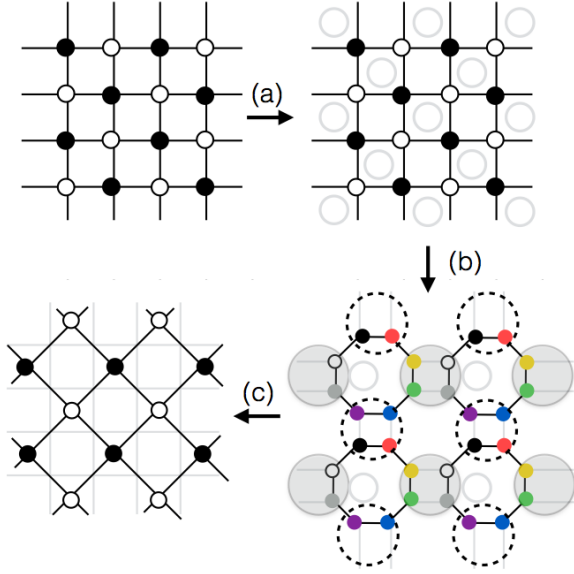


FIG. 23. Schematic procedure of the Loop-TNR procedure in 2d. (a) We remove local entanglement on alternating plaquettes, labeled with grey circles, by inserting projectors. (b) We convert these square plaquettes into octagon plaquettes made up of eight rank-3 tensors and optimize them. (c) We form new tensors by contracting the tensors in the grey and dotted circles, as in the standard tensor renormalization group (TRG) procedure proposed by Levin and Nave.

and that when we apply this analysis to a 2D quantum system, the universal data  $c$ ,  $\Delta_\alpha$ , and  $s_\alpha$  that we extract describe the infrared limit of the doubled vertex model and not the quantum model. However, with caution we can draw limited conclusions from it, as follows. Correlators of local operators in the quantum state can as in Fig. 3 be expressed as correlators of local operators in the doubled vertex model, which means at least that quasi-long-range order in the quantum model implies quasi-long-range order in the doubled vertex model. Thus when we find that the doubled vertex model is *not* critical, we determine that the quantum model has finite correlation length and is likely gapped. Conversely, when we find that the doubled vertex model *is* critical, we seek operators on the quantum model whose correlations correspond to those predicted by the classical scaling dimensions; when we find them, we conclude that the quantum model has infinite correlation length and thus is gapless.<sup>48,49</sup>

#### 4. Loop optimization for tensor network renormalization

As with the above TNR procedure, loop optimization for tensor network renormalization (loop-TNR), proposed by Yang, Gu, and Wen<sup>50</sup>, has the goal of removing local entanglement in order to obtain a renormalization-

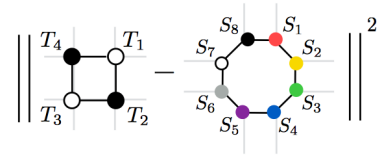


FIG. 24. The cost function for optimizing loop-TNR tensors

group fixed point in tensor form. This approach is a real-space renormalization procedure based on the existing TRG procedure<sup>29</sup> of Levin and Nave, modified by removing short-range entanglement at the start of the procedure and optimizing intermediate tensors in loops. We may apply it to classical and quantum systems in much the same circumstances as Evenbly and Vidal’s TNR. The details of the algorithm, as sketched in Fig. 23, are as follows:

1. Starting with a tensor contraction on a square lattice as in Fig. 23(a), we put each tensor into a canonical form by inserting “projectors” which filter out local entanglement onto the bonds around plaquettes. These projectors are constructed iteratively using QR decomposition.
2. We then deform the tensor network from a square lattice to a square-octagon lattice by performing a truncated singular-value decomposition, as in Levin and Nave’s TRG, to approximate each rank-4  $T_i$  tensor as the contraction of a pair of rank-3 tensors  $S_i$ . This is shown in Fig. 23(b).
3. We then optimize the  $S_i$  in an octagonal loop by minimizing the cost function in Fig. 24.
4. Finally, as in standard TRG, we contract the four tensors around each square plaquette of the square-octagon lattice [Fig. 23(c)]. These plaquettes become the sites of a new, coarse-grained square lattice, with half as many sites as the original lattice.

#### 5. Explicit form of the PEPS tensors

For completeness we state the exact form of the tensors which comprise the state primarily considered in this work, i.e., the spin-2 state, situated on a lattice with coordination number  $q = 4$ . If the state has deformation  $a_1, a_2$  and bond state  $|\psi^-\rangle$ , the tensors have nonzero el-

ements

$$\begin{aligned}
A_{\uparrow\uparrow\uparrow\uparrow}^2 &= a_2, \quad A_{\uparrow\uparrow\uparrow\downarrow}^1 = A_{\uparrow\uparrow\downarrow\uparrow}^1 = A_{\uparrow\downarrow\uparrow\uparrow}^1 = A_{\downarrow\uparrow\uparrow\uparrow}^1 = a_1 \\
A_{\downarrow\downarrow\downarrow\downarrow}^{-2} &= a_2, \quad A_{\downarrow\downarrow\downarrow\uparrow}^{-1} = A_{\downarrow\downarrow\uparrow\downarrow}^{-1} = A_{\downarrow\uparrow\downarrow\downarrow}^{-1} = A_{\uparrow\downarrow\downarrow\downarrow}^{-1} = a_1 \\
A_{\uparrow\uparrow\downarrow\downarrow}^0 &= A_{\uparrow\downarrow\downarrow\uparrow}^0 = A_{\downarrow\downarrow\uparrow\uparrow}^0 = A_{\downarrow\uparrow\uparrow\downarrow}^0 = A_{\uparrow\downarrow\uparrow\downarrow}^0 = A_{\downarrow\uparrow\downarrow\uparrow}^0 = a_0
\end{aligned} \tag{A4}$$

$$\begin{aligned}
B_{\downarrow\downarrow\downarrow\downarrow}^2 &= a_2, \quad B_{\downarrow\downarrow\downarrow\uparrow}^1 = B_{\downarrow\downarrow\uparrow\downarrow}^1 = B_{\downarrow\uparrow\downarrow\downarrow}^1 = B_{\uparrow\downarrow\downarrow\downarrow}^1 = -a_1 \\
B_{\uparrow\uparrow\uparrow\uparrow}^{-2} &= a_2, \quad B_{\uparrow\uparrow\uparrow\downarrow}^{-1} = B_{\uparrow\uparrow\downarrow\uparrow}^{-1} = B_{\uparrow\downarrow\uparrow\uparrow}^{-1} = B_{\downarrow\uparrow\uparrow\uparrow}^{-1} = -a_1 \\
B_{\uparrow\uparrow\downarrow\downarrow}^0 &= B_{\uparrow\downarrow\downarrow\uparrow}^0 = B_{\downarrow\downarrow\uparrow\uparrow}^0 = B_{\downarrow\uparrow\uparrow\downarrow}^0 = B_{\uparrow\downarrow\uparrow\downarrow}^0 = B_{\downarrow\uparrow\downarrow\uparrow}^0 = a_0,
\end{aligned} \tag{A5}$$

where tensors  $A$  and  $B$  are placed on alternating sublattices.

## Appendix B: The general Hamiltonian and the spin-1 analogy

### 1. Niggeman, Klümper, and Zittartz's Hamiltonian

In the original work by Niggeman, Klümper, and Zittartz<sup>10</sup> a general two-site Hamiltonian, invariant under spin flips and  $S_z$  rotations (that is, the same  $O(2)$  symmetry of the deformed-AKLT model) as well as spatial symmetries, is presented in Eqs. (3)-(5). The valence-bond construction they proceed to define in Eq. (8)-(10) is equivalent to our deformed-AKLT state. There the parameters  $a$  and  $b$  correspond to  $a_1$  and  $a_2$ , respectively, in our work, and  $\sigma$  specifies the bond state: We will set  $\sigma = 1$ , corresponding to the antiferromagnet singlet bond state  $|\psi^-\rangle$ . The 22-parameter Hamiltonian of Eq. (7) then, as in Eqs. (12) and (13), becomes the seven-parameter Hamiltonian

$$\begin{aligned}
h_{ij} &= \lambda_4 (|v_4\rangle\langle v_4| + |v_{-4}\rangle\langle v_{-4}|) \\
&+ \lambda_3^+ (|v_3^+\rangle\langle v_3^+| + |v_{-3}^+\rangle\langle v_{-3}^+|) \\
&+ \lambda_{22}^+ (|v_{22}^+\rangle\langle v_{22}^+| + |v_{-22}^+\rangle\langle v_{-22}^+|) \\
&+ \lambda_{12}^+ (|v_{12}^+\rangle\langle v_{12}^+| + |v_{-12}^+\rangle\langle v_{-12}^+|) \\
&+ \lambda_{03}^+ (|v_{03}^+\rangle\langle v_{03}^+|)
\end{aligned} \tag{B1}$$

$$|v_{\pm 4}\rangle = |\pm 2, \pm 2\rangle \tag{B2}$$

$$|v_{\pm 3}^+\rangle = |\pm 1, \pm 1\rangle + |\pm 2, \pm 1\rangle \tag{B3}$$

$$|v_{\pm 22}^+\rangle = \frac{a_2}{a_1} |\pm 1, \pm 2\rangle - (|0, \pm 2\rangle + |\pm 2, 0\rangle) \tag{B4}$$

$$|v_{\pm 12}^+\rangle = a_2 (|0, \pm 1\rangle + |\pm 1, 0\rangle) - (|\mp 1, \pm 2\rangle + |\pm 2, \mp 1\rangle) \tag{B5}$$

$$\begin{aligned}
|v_{03}^+\rangle &= |0, 0\rangle + \frac{1}{a_1} (|+1, -1\rangle + |-1, +1\rangle) \\
&+ \frac{1}{a_2} (|+2, -2\rangle + |-2, +2\rangle)
\end{aligned} \tag{B6}$$

Of these seven parameters, two are the deformation parameters  $a_1$  and  $a_2$ . Meanwhile a rescaling of the remaining five,  $\lambda_4, \lambda_3^+, \lambda_{22}^+, \lambda_{12}^+, \lambda_{03}^+$ , is simply an energy rescaling. Noting that energy shifts are already accounted for,

as the minimal eigenvalue of  $h_{ij}$  is fixed at 0, we find that, in this formulation, we have a four-parameter family of distinct parent Hamiltonians for *every* deformed-AKLT state  $|\Psi(a_1, a_2)\rangle$  (with  $0 < a_1, a_2 < \infty$ ).

Comparing this with the form of the Hamiltonian in (6), we determine that, for a given value of the deformation parameters  $a_1$  and  $a_2$ , these two Hamiltonians will be equal when we set

$$\begin{aligned}
\lambda_{03}^+ &= \frac{18}{35} \\
\lambda_{12}^+ &= \frac{9}{14a_1^2 a_2^2} \\
\lambda_{22}^+ &= \frac{9}{7a_2^2} \\
\lambda_3^+ &= \frac{9}{2a_1^2 a_2^2} \\
\lambda_4 &= \frac{36}{a_2^4}.
\end{aligned} \tag{B7}$$

### 2. Explanation of the XY phase

In the continuum path integral approach Haldane adopts for antiferromagnets<sup>16</sup>, we note that we can emulate the deformation by inserting a zero-time ‘‘projection’’ factor into the semiclassical AKLT partition function:

$$Z_{(a_1, a_2)} \simeq \int \mathcal{D}[\vec{\Omega}] e^{i\Upsilon[\vec{\Omega}]} e^{-\mathcal{S}_{\text{AKLT}}[\vec{\Omega}, \vec{L}]} P_{(a_1, a_2)}[\vec{\Omega}] \tag{B8}$$

$$P_{(a_1, a_2)}[\vec{\Omega}] \equiv \prod_{v \in V} p_{(a_1, a_2)}(\theta(t=0, \vec{r}=v)) \tag{B9}$$

where  $\vec{\Omega}$  is the Néel field,  $\vec{L}$  is the net spin density,  $\Upsilon$  is the Berry phase arising from  $\vec{\Omega}$ ,  $\mathcal{S}_{\text{AKLT}}$  is the AKLT action (as a continuum approximation),  $\theta$  is the zenith angle corresponding to the unit vector  $\Omega$ , and  $p_{\vec{a}}(\theta)$  is a function of  $\theta$  (even under  $\theta \rightarrow \pi - \theta$ ) which represents the deformation  $D(\vec{a})$  as follows:

$$D(\vec{a})^2 = \int d\Omega p_{\vec{a}}(\theta) |\Omega\rangle\langle\Omega|. \tag{B10}$$

This does not uniquely specify  $p_{\vec{a}}$ ; in fact, any suitable three-parameter ansatz should provide a solution within some region of phase space. For example, if we anticipate a low-order polynomial in  $\cos \theta$ , we find

$$\begin{aligned}
p_{(a_1, a_2)}(\theta) &= \frac{5}{4} (19 - 168 \cos \theta + 189 \cos^2 \theta) \\
&+ (-15 + 175 \cos \theta - 210 \cos^2 \theta) a_1^2 \\
&+ \frac{5}{8} (1 - 70 \cos \theta + 105 \cos^2 \theta) a_2^2
\end{aligned} \tag{B11}$$

Although this particular ansatz is not especially illustrative, we hope that we can represent the deformation in some way such that, for  $a_1, a_2 \rightarrow 0$ ,  $P$  restricts zero-time

configurations towards the easy plane  $\theta = \frac{\pi}{2}$ , so that valid configurations primarily remain in a band around the equator. In this case the azimuthal angle  $\phi$  at zero time should resemble a classical XY rotor. Should that rotor belong to the low-temperature phase, described in the infrared by a compactified-free-boson CFT with some coupling  $g > 4$ , then its most relevant scaling operator will be a vertex operator  $V_{\pm 1,0}(z) \propto :e^{\pm i\phi(z)}:$ . The latter expression translates into the coherent-spin framework as

$$\int d\Omega e^{\pm i\phi} |\Omega\rangle\langle\Omega| = \eta \frac{4\pi}{15} (S_x \pm iS_y). \quad (\text{B12})$$

where  $\eta = \pm 1$  is a sign that indicates alternating sublattices.

### 3. XY vortices and tunneling processes

We refer to our hypothesis in Sec. IIID that the XY phase can be explained as coherent-spin rotors at an imaginary-time 0 surface at which the deformation restricts spins away from the poles. We then consider the Kosterlitz-Thouless transition, effected by the condensation of vortices in these rotors. Given such a  $\tau = 0$  vortex configuration, we suggest that the dominant coherent-spin configurations contributing to it will be tunneling processes, short-lived discontinuities in the spin-wave configurations which are integrated over in the coherent-spin path integral. We can view such configurations as vortices being created and then dissipating; thus our claim is that that a vortex in the azimuthal angle on the  $\tau = 0$  plane corresponds to a tunneling process occurring at  $\tau \sim 0$  with the configuration returning to a smoothly-varying spin wave sufficiently far from  $\tau \sim 0$ .

Now we refer to Haldane's analysis<sup>16</sup> of topological effects in  $SU(2)$  antiferromagnets in 2D. His conclusion is that tunneling processes provide the basis for the following distinction between even-integer and odd-integer spin systems: In odd-integer spin systems, tunneling processes change the sign of the Berry-phase factor when moved by one site; thus, when one such process is sufficiently isolated from all others that this change will not significantly affect the action, that configuration will cancel with one in which the tunneling process in question has been moved by one site. Thus, when we see the kind of XY-like behavior observed in the deformed-AKLT system, if the spin is *odd*-integer, then we expect the winding-number-1 vortices that become relevant at coupling  $g = 4$  to correspond to tunneling processes isolated either in space or imaginary time and therefore prohibited by these topological considerations. Instead, only even-winding-number vortices, corresponding to bound pairs of tunneling processes, will contribute to the path integral. As the first of these,  $V_{0,\pm 2}$ , becomes relevant at  $g = 1$ , the XY-like phase will remain stable for all  $g > 1$  and the Kosterlitz-Thouless transition will only occur at  $g = 1$ . For *even*-integer systems, meanwhile, the Berry

phase is trivial for all mostly-smooth configurations, so no tunneling processes will be excluded.

### 4. Explaining pseudo-quasi-long-range ordered behavior

The square-lattice deformed-AKLT system studied herein is manifestly spin-2; in particular, as described above, we can express it in path-integral form as the spin-2,  $SU(2)$ -invariant AKLT path integral with a planar deformation operator inserted at imaginary time  $\tau = 0$ . Here we suggest that, along the  $a_2 = 0$  boundary of the phase diagram, the system may be similarly approximated as a deformation of a spin-1 antiferromagnet; in particular, that, when we examine the  $a_2 \rightarrow 0$  limit of the Hamiltonian and extract the effective Hamiltonian at leading order in perturbation theory, for some value of  $a_1$  this will be a spin-1  $SU(2)$ -invariant antiferromagnet. Though it is not immediately clear how, or if, this may best be done rigorously, we state it as an expectation based on intuitive observations of, for example, the “spin-1”  $O(2)$  transformation properties obeyed along this line, and confirmed by the system's behavior.

If we can find such a relationship to a spin-1 system, Haldane's nonlinear sigma model argument discussed above implies that this system will lack isolated tunneling processes in its path integral, suppressing any isolated vortices that would arise in the  $\tau = 0$  rotor configuration, as above. In the deformed-AKLT model, therefore, we anticipate an *approximate* relationship between the  $a_2 = 0$  limit and this system which demonstrates vortex suppression, and, therefore, a likewise approximate suppression of isolated vortices. Thus, while we find that XY vortices still become *relevant* when  $g < 4$ , they are approximately suppressed and therefore only become apparent at large length scales. In particular, we propose this approximate spin-1 physics as an explanation for the “pseudo-quasi-long-range order” we observe near the  $a_2 = 0$  axis, in that very large but finite correlation lengths are caused by relevant perturbations that remain very small far from the phase transition.

### Appendix C: Phase transitions from tracking critical data

As the data summarized in Fig. 9 suggests, we find that the most distinctive way to identify and track the Berezinskii-Kosterlitz-Thouless-like transition(s) observed at the boundary or boundaries of the XY phase is to follow TNR estimates of  $c$  and  $g$  along lines in the phase diagram which cross these boundaries. By plotting these estimates at successive coarse-graining steps, we find that inside the XY region, estimates of  $c$  and  $g$  both converge to nontrivial asymptotic values:  $c \simeq 1$ , while  $g \geq 4$  but varies continuously with the deformation parameters. Outside of that region, estimates for  $g$  fall

towards 0 and estimates for  $c$  eventually follow suit. By determining the parameters at which  $g$ , at some length scale, drops below 4, we can find the boundaries of the XY phase. In Fig. 25 we see that we can use this to define the XY-AKLT transition as well as the pseudo-quasi-long-range ordered region. (Some points of the transition explored in Fig. 25 have been probed in more detail in Fig. 12.) In Fig. 26, meanwhile, we see that a similar transition occurs as we approach the origin from within the XY phase; it is almost as clear as the transition into the AKLT phase, but it recedes to the origin as bond dimension is increased.

#### Appendix D: Using bond-dimension comparisons to analyze the product-state region

By comparing estimates of  $c$  and  $g$  at each coarse-graining step, we observe how increasing the bond dimension used during TNR affects our estimates of the system's behavior near the origin. In Fig. 27 we see that even the exactly-understood  $c = 2$  behavior at the origin is difficult to replicate with TNR. Similar behavior also appears in Fig. 33, although then it is at a point spaced reasonably far along the  $a_1 = 0$  axis. Figures 28, 29, and 30 demonstrate that, where we see  $g$  take an asymptotic value in the thermodynamic limit, that limiting value will typically increase as we raise the bond dimension. Figures 31 and 32 suggest that numerical inadequacies at relatively short length scales may sharply influence what kind of infrared behavior we observe. Finally, through Fig. 34, we conclude that the methods used in this work are inconclusive as to the system's behavior in the innermost part of this region, when  $a_2 < 0.2$  and  $a_1 \ll 0.01$ .

#### Appendix E: The critical exponent $\delta$

At a point of the phase diagram we believe to be critical, we may investigate another critical exponent: Given a sufficiently small applied field  $h$ , we expect to find magnetization  $m$  such that<sup>51</sup>

$$h \propto m^\delta, \quad \delta = \frac{2 - \Delta}{\Delta} = 4g - 1. \quad (\text{E1})$$

We will implement the field  $h$  by perturbing the wavefunction, simultaneously applying  $\exp(hS_{\phi_A})$  to every site of sublattice  $A$  and  $\exp(hS_{\phi_B})$  to every site of sublattice  $B$ . Here  $\phi_A$  and  $\phi_B$  may in principle differ and the difference  $\phi_A - \phi_B$  may control the magnitude of the effect. Then  $m$  is the expectation value of  $S_{\phi_A}$  at a site in sublattice  $A$ . This changes the weight matrix of the doubled vertex model in a manner we might expect from a magnetic field; as for the quantum model, though,

this reflects not one-site perturbations of the form  $hS_\phi^{(i)}$  as we might expect, but rather  $h\{S_\phi^{(i)}, H_{i,j}\}$  obtained by deforming the Hamiltonian as in (6). It is, nonetheless,

physical, and can therefore be used to confirm quasi-long-range order of the quantum state. When we investigate this quantity (using HOTRG), we find in Fig. 35 that the response of an order parameter to a ‘‘magnetizing’’ perturbation fits a power-law curve as expected. From this curve we can obtain a value of  $\delta$  through linear regression. Then, as we increase the system size, this value rapidly converges. When the perturbation is at the same angle on both sublattices, the order parameter responds less predictably to perturbations. Otherwise it behaves in a way indicative of criticality, and as we increase bond dimension the limiting value of  $\delta$  approaches the expected  $4g - 1$ , with  $g$  obtained through TNR.

We can also use  $\delta$  to study the Kosterlitz-Thouless transition. Following it as in Fig. 36, we find that it appears to be smooth across the phase transition, approximating the TNR value of  $g$  on the critical side while taking a value of uncertain significance on the AKLT side. We can use this to find the transition by looking for  $g_\delta = 4$ . Admittedly, this only indicates a transition if we accept *a priori* that the transition will occur at  $g = 4$ .

#### Appendix F: The corner entropy

We here use CTMRG to extract the corner entropy described in Appendix A 1. We expect that this quantity will be singular at phase transitions and therefore can be used to predict the boundary of phases. However, we note that, as the doubled vertex model is critical throughout the XY region, the corner entropy should diverge throughout this region. Since these estimates are limited by bond dimension, they will not be precise at any point there.

In Fig. 39, we see how we can extract the corner entropy and use it to get estimates for the transitions both into the XY and Néel-ordered phases. Fig. 37 demonstrates that these estimates are fairly robust along the  $a_2$  axis. In Fig. 38, however, we see by increasing bond dimension that the phase boundary obtained through this method is much less robust in the pseudo-quasi-long-range ordered region. In particular we suggest that the boundary at some fixed bond dimension may roughly demark the pseudo-quasi-long-range ordered region.



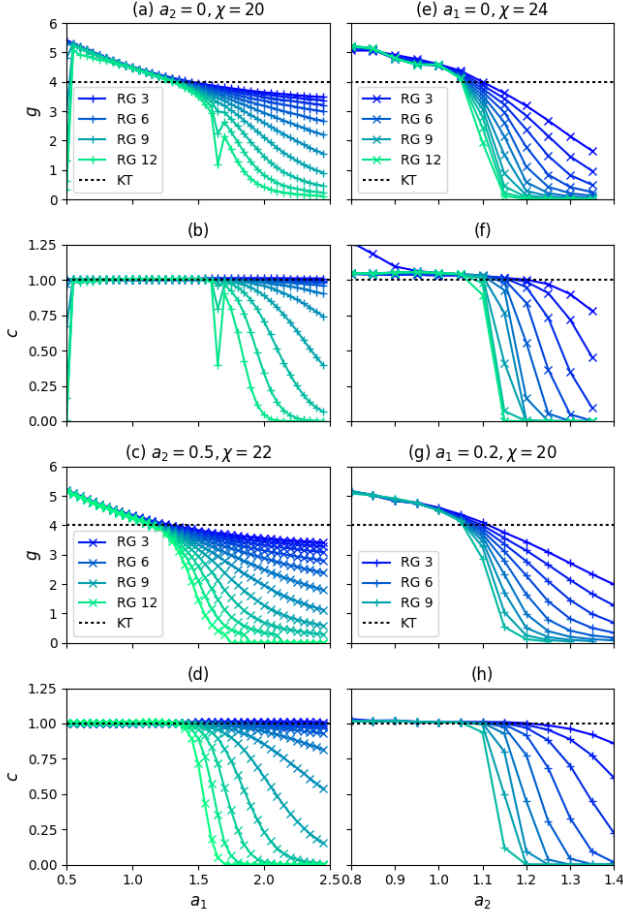


FIG. 25. We follow  $c$  and  $g$  along lines of the phase diagram which pass through the Kosterlitz-Thouless-like transition from the XY phase to the AKLT phase. (a),(b) On the axis  $a_2 = 0$ ,  $g$  steadily decreases with increasing  $a_1$  until  $a_1 \simeq 1.25$ , where a KT transition appears to occur. (c),(d) We observe much the same behavior on the  $a_2 = 0.5$  line, although here the transition is closer to  $a_1 = 1.15$ . (Here we see some instability, characteristic of the choice to preserve  $\mathbb{Z} \times \mathbb{Z}$  rather than some larger subgroup of  $O(2)$ ). (e),(f) We see a similar transition occur when we increase  $a_2$  along the  $a_1 = 0$  axis, with  $g$  dropping below 4 by  $a_2 = 1.1$ . Here, however, the transition is much sharper, indicating that the correlation length when displaced by  $\Delta a_2 \simeq 0.05$  from the transition in (f) - that is, roughly  $\xi \sim 300$  at  $a_1 = 0$ ,  $a_2 = 1.25$  - is as much or less than that at  $\Delta a_1 \simeq 1.0$  from the transition in (b) or (d), as for example  $\xi \sim 300$  at  $a_1 = 2.2$ ,  $a_2 = 0.5$ . This conclusion is consistent with Figs. 1 and 14 in its implications for a pseudo-quasi-long-range ordered region. (g),(h) If we move slightly, to  $a_1 = 0.2$ , we see a much clearer picture of a similarly sharp transition at approximately the same value of  $a_2$ .

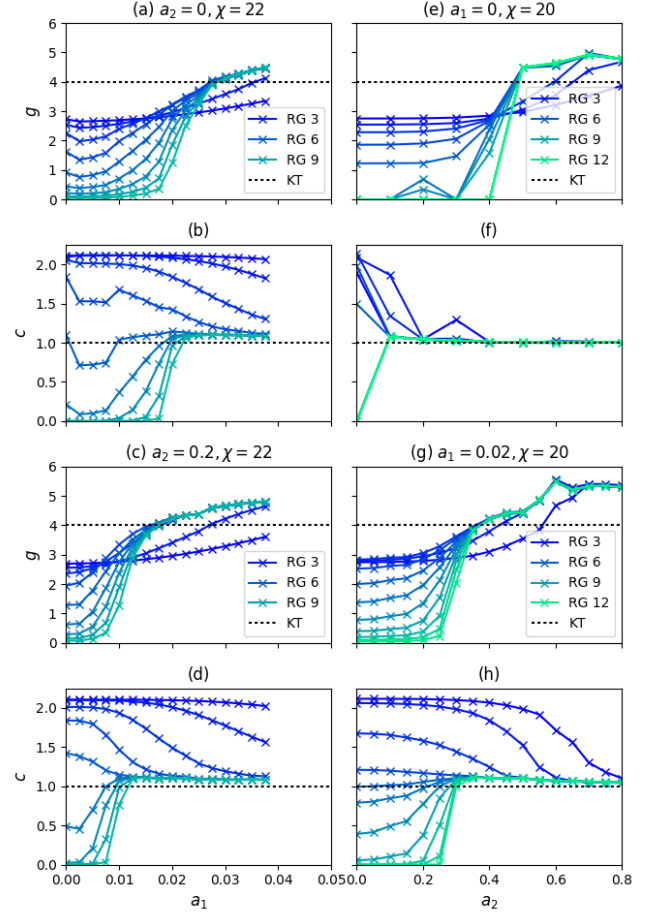


FIG. 26. As we approach the origin with fixed bond dimension, we find that estimates of  $c$  and  $g$  behave much like they do in Fig. 25 when they cross the KT transition into the AKLT phase, although here the data are somewhat noisier and harder to discern patterns from. (a),(b) On the  $a_2 = 0$  axis, with  $\chi = 22$ , we observe a transition at approximately  $a_1 = 0.028$ . (c),(d) When we move to  $a_2 = 0.2$ , this transition shifts to about  $a_1 = 0.017$ . (e),(f) Conversely, on the  $a_1 = 0$  axis with  $\chi = 20$ , we see evidence of a transition around  $a_2 = 0.45$ . (g),(h) But when we move to just  $a_1 = 0.02$ , it shifts closer to  $a_2 = 0.23$ .

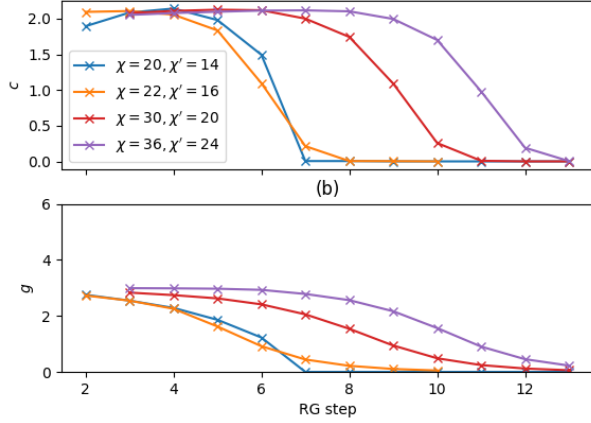


FIG. 27.  $a_1 = 0, a_2 = 0$ : At the origin, we know that, theoretically,  $c = 2$  and  $g = 3$  exactly. While increasing the bond dimension allows us to approximate these numbers at larger length scales, even with  $\chi = 36$ , TNR estimates do not remain stable.

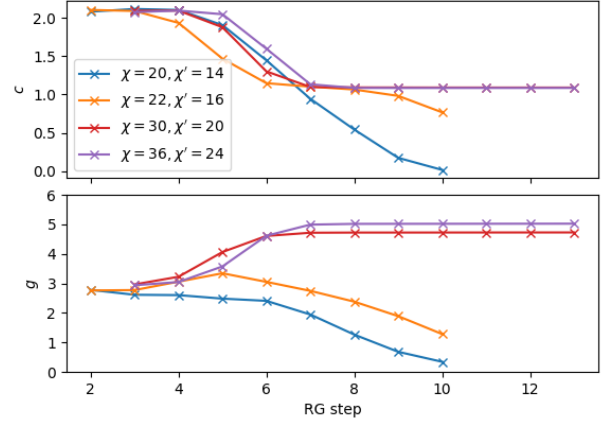


FIG. 29.  $a_1 = 0.01, a_2 = 0.2$ : Here the system exhibits XY-like behavior at  $\chi = 30, \chi' = 20$ ; raising the bond dimension to  $\chi = 36, \chi' = 24$  again increases the estimated value of  $g$ .

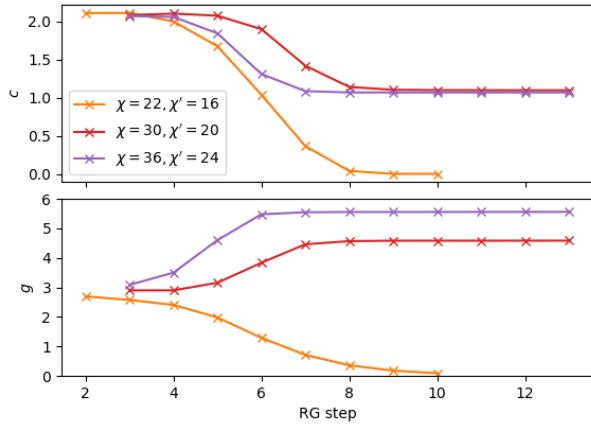


FIG. 28.  $a_1 = 0.01, a_2 = 0$ : Here the system exhibits XY-like behavior at  $\chi = 30, \chi' = 20$ ; raising the bond dimension to  $\chi = 36, \chi' = 24$  increases the estimated value of  $g$  substantially.

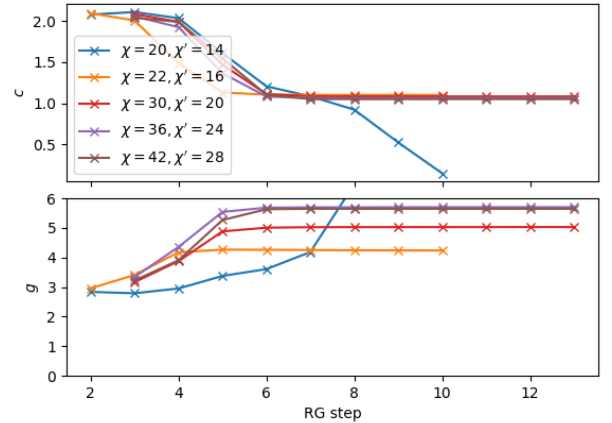


FIG. 30.  $a_1 = 0.02, a_2 = 0.2$ : Here the system exhibits XY-like behavior with bond dimension as low as  $\chi = 22, \chi' = 16$ ; the estimated asymptotic value of  $g$  increases when raising the bond dimension to  $\chi = 30, \chi' = 20$  and again in raising it to  $\chi = 36, \chi' = 24$ ; however, it appears to be stable when the bond dimension increases to  $\chi = 42, \chi' = 28$ .

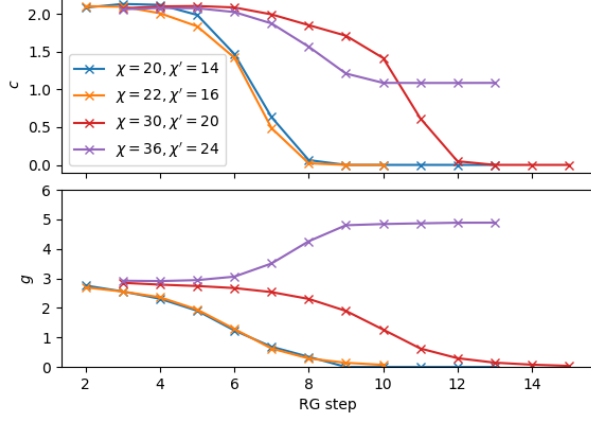


FIG. 31.  $a_1 = 0, a_2 = 0.2$ : While the system does not exhibit XY-like behavior for bond dimension  $\chi = 30, \chi' = 20$ , this changes when we increase the bond dimension to  $\chi = 36, \chi' = 24$ . Tracking  $g$  and  $c$ , we find that they diverge at the crossover from  $c = 2$  behavior: with lower bond dimension, the  $c$  large,  $g$  small behavior draws out until larger length scales before proving unstable, while for higher bond dimension,  $c$  more quickly falls to 1 and  $g$  more quickly rises to about 5.

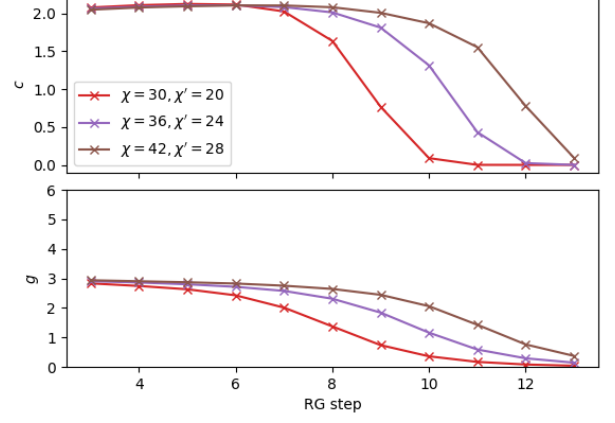


FIG. 33.  $a_1 = 0, a_2 = 0.1$ : At this point relatively close to the origin along the  $a_1 = 0$  line, we observe behavior similar to that of Fig. 27 as we increase the bond dimension to  $\chi = 42, \chi' = 28$ . At no point do we see behavior consistent with the XY phase.

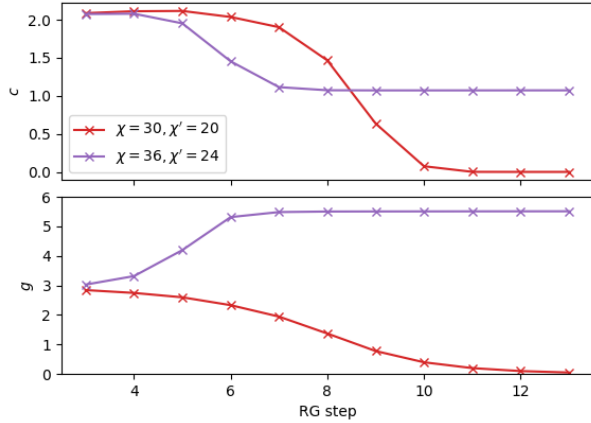


FIG. 32.  $a_1 = 0.001, a_2 = 0.001$ : Here, very close to the origin, we see behavior similar to that in Fig. 27 for  $\chi = 30, \chi' = 20$ , but raising the bond dimension to  $\chi = 36, \chi' = 24$  we again see that a crossover into XY-like behavior appears. As in Fig. 31, this suggests that the effects that make the difference in these cases are short to medium-range, in particular less than 100 sites.

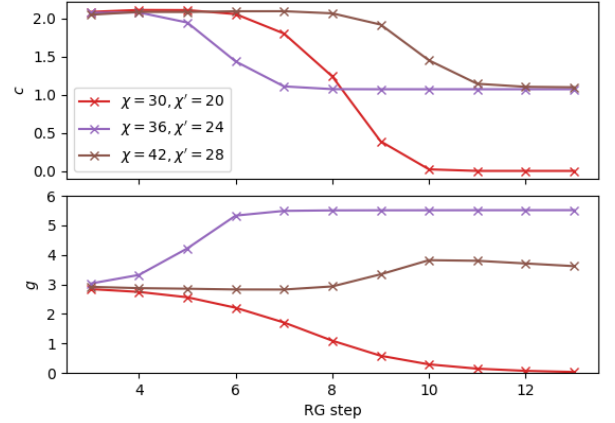


FIG. 34.  $a_1 = 0.001, a_2 = 0.05$ : Here we have estimates from  $\chi = 30, \chi' = 20, \chi = 36, \chi' = 24$ , and  $\chi = 42, \chi' = 28$ , none of which are mutually consistent.  $\chi = 30, \chi' = 20$  suggests product-state behavior;  $\chi = 36, \chi' = 24$  suggests XY-like behavior; and  $\chi = 42, \chi' = 28$  demonstrates a crossover from  $c = 2$  to  $c = 1$  behavior with an unstable value of  $g$ . We conclude that the bond dimensions which we are capable of employing are inadequate at this point.

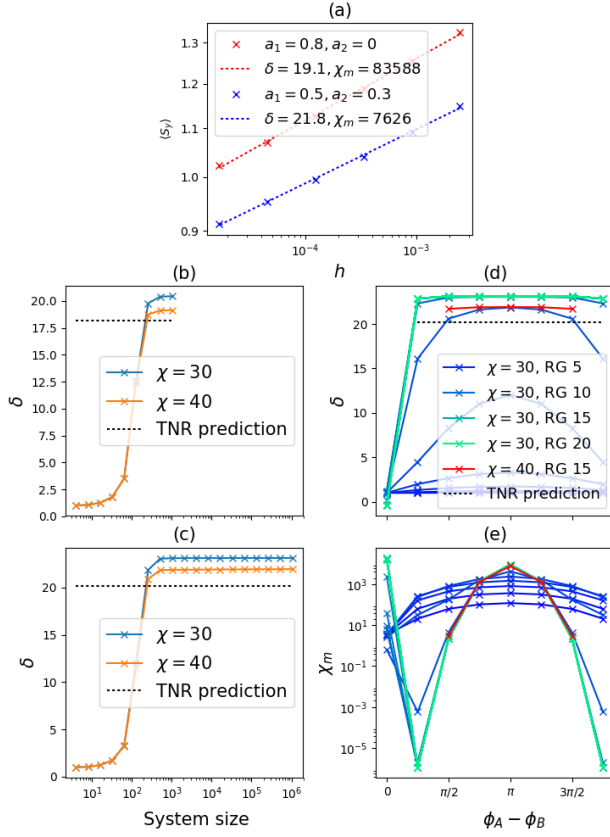


FIG. 35. Using the critical exponent  $\delta$ , describing response to a symmetry-breaking perturbation, to examine quasi-long-range order. (a) Sample fitting of the ansatz  $m^\delta = \chi_m h$ , with  $\chi = 40$  and linear system size  $2^{10}$ , perturbations on different sublattices being separated by relative angle  $\pi$ . (b),(c) As we increase the system size, the fitted value of  $\delta$  increases to an asymptotic value. Then, as we increase the bond dimension, this value approaches the  $4g - 1$  we expect from TNR. (d) When we vary the angle between sublattice perturbations, we find that  $\delta$  approaches the same value - quickly enough that the data from most coarse-graining steps are indistinguishable - for any relative angle except 0, where the ansatz does not fit as well.<sup>a</sup> (e) Additionally, at angles where the ansatz does fit, the response coefficient that we call  $\chi_m$  is greatest when  $\phi_A - \phi_B = \pi$  and falls off dramatically approaching  $\phi_A - \phi_B = 0$ .

<sup>a</sup> Note in particular that the amplitude of the response does not “blow up” at  $\phi = 0$  as it may appear from (e); for  $m = \chi^{1/\delta} h^{1/\delta}$  and an anomalous value  $\delta \sim 0$ , a very large  $\chi$  corresponds to a more tempered response.

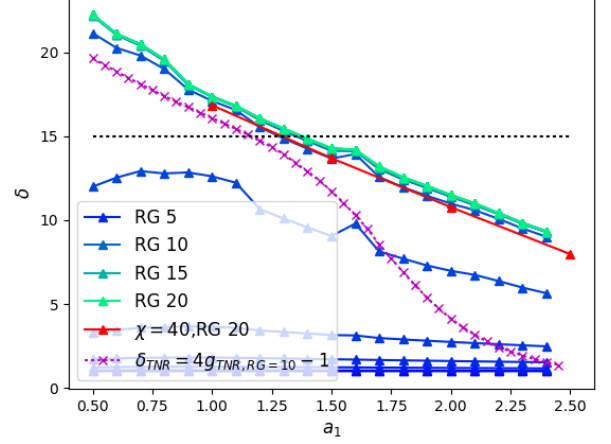


FIG. 36. We use HOTRG with  $\chi = 30$  to estimate the value of the critical exponent  $\delta$  on both sides of the KT transition, along the line  $a_2 = 0.5$ . On the critical side, its asymptotic value follows roughly what we would expect from the TNR data of Fig. 25, and approaches that value when we increase  $\chi$  to 40. On the AKLT side of the transition, however, we find that the  $\delta$  versus  $a_1$  curve appears to remain approximately straight rather than falling to a trivial value, and that corrections from increasing the bond dimension only shift the line rather than changing its behavior.

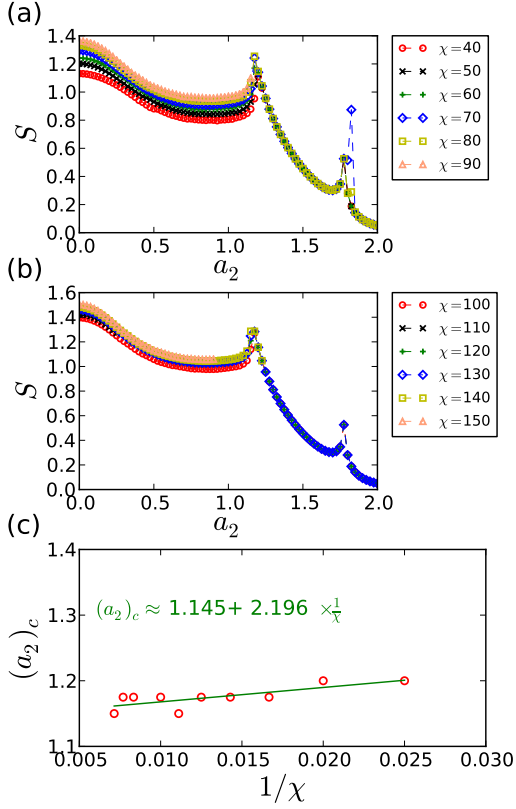


FIG. 37. We extract the corner entropy for the norm of the deformed-AKLT state on the square lattice as a function of the parameter  $a_2$  on the  $a_1 = 0.0$  axis, varying the bond dimension (a) from 40 to 100 (b) from 110 to 150. (c) We extrapolate the location  $(a_2)_c$  of the KT transition on this line in the limit of large bond dimension  $\chi^{-1} \rightarrow 0$ . Extrapolation from a linear fit suggests that the critical point is at  $(a_2)_c \simeq 1.145$ , a reasonable approximation of the TNR estimate  $(a_2)_c \simeq 1.10$ . We note generally that both critical points are fairly robust under increases in bond dimension, although the corner entropy in the XY region generally keeps increasing as the bond dimension increases, as expected since the true value should not be finite.

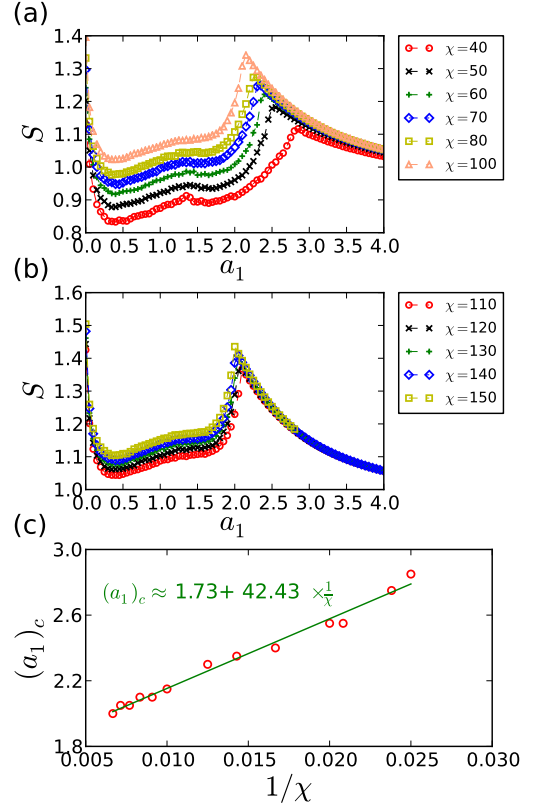


FIG. 38. We extract the corner entropy as a function of the parameter  $a_1$  on the  $a_2 = 0.0$  axis, varying the bond dimension (a) from 40 to 100 (b) from 110 to 150. (c) We extrapolate the location  $(a_1)_c$  of the KT transition along this line in the limit of large bond dimension  $\chi^{-1} \rightarrow 0$ . Extrapolating from a linear fit suggests that the critical point is at  $(a_1)_c \simeq 1.73$ . This is not a particularly reasonable approximation of the TNR estimate  $a_1 \simeq 1.30$ ; in fact, we note that the estimates of  $(a_1)_c$  using this method have not begun to converge, even with high bond dimension  $\chi = 150$ . As we do not expect CTMRG to accurately approximate systems with the very large correlation length observed in the pseudo-quasi-long-range ordered region, this is also not surprising.

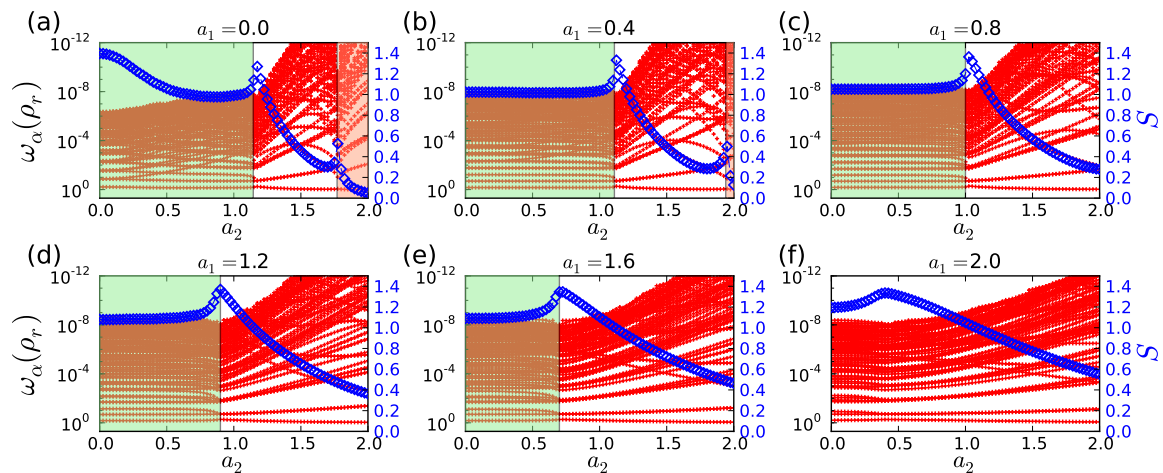


FIG. 39. We plot the corner entanglement spectra  $\omega_\alpha$  (red) and the corner entropy (blue) for the norm of the square-lattice deformed-AKLT state as a function of the parameter  $a_2$  with (a)  $a_1 = 0.0$ , (b)  $a_1 = 0.4$ , (c)  $a_1 = 0.8$ , (d)  $a_1 = 1.2$ , (e)  $a_1 = 1.6$ , and (f)  $a_1 = 2.0$ , obtained using CTMRG with bond dimension  $\chi = 100$ . We find sharp phase transitions from the AKLT phase into the XY and Néel-ordered phases. Close to the  $a_2$  axis, in (a) and (b), we see agreement with the phase boundaries obtained elsewhere. However, (d)-(f) demonstrate that, in the pseudo-quasi-long-range ordered region, this method does not accurately reflect the results obtained with TNR. This is somewhat expected as the bond dimension of CTMRG effectively limits the correlation length of systems it can effectively simulate.

### Appendix G: Operator content of critical points

When we find using TNR that a 2D classical theory reaches approximate scale invariance under coarse-graining, we can estimate the operator content of the CFT that may arise in the infrared limit. In Figs. 40 and 41, we use data from TNR with  $\chi = 26$ ,  $\chi' = 16$  after the twelfth coarse-graining step. Data (black  $\times$ s) is extracted by diagonalizing a transfer matrix of three coarse-grained sites; the range of conformal spins is increased by approximating a 6-site transfer matrix as in Appendix B of Hauru et al.<sup>45</sup> Since the latter approximation yields much less accuracy for scaling dimensions, we attempt to plot scaling dimensions from 3-site data with conformal spins from the 6-site approximation, but these datasets are occasionally mismatched.

Preserving  $D_{2N}$  symmetry allows us to separately diagonalize blocks of the transfer matrix which correspond to irreducible representations of the on-site  $O(2)$  symmetry.<sup>52</sup> We then construct separate plots, for each irrep, of the scaling dimension and conformal spin of scaling operators that transform under it (excluding  $k > 6$

irreps, for which the data would not appear within the axes we have chosen).

We also use the smallest scaling dimension of charge  $k = 1$  to estimate  $g$ , as expressed in Fig. 10, and from there, we plot our estimates of the conformal tower based on that value of  $g$ : Blue circles correspond to scaling operators with no “magnetic” charge, whereas red circles correspond to scaling operators with magnetic charge  $m = \pm 1$  (scaling operators with  $|m| > 1$  should have  $\Delta \geq 8$ , and therefore should lie outside the range of these plots). In doing so we find excellent agreement from the data: In (a), we plot data from states that transform under the trivial representation of  $O(2)$  and find the descendants of the identity and of the first “vortex” operator  $V_{0,1} + V_{0,-1}$ . In (b), we plot data from states which have no  $U(1)$  charge but have odd parity under  $O(2)$  reflections, and see the  $\partial, \bar{\partial}$  operators and their descendants, as well as the vortex operator  $V_{0,1} - V_{0,-1}$ . In (c)-(h), we see the “electric” operators  $V_{\pm e,0}$  as well as the operators  $V_{\pm e,\pm 1}$  which have both “electric” and “magnetic” charge.

<sup>1</sup> F. D. M. Haldane, Phys. Rev. Lett. **50**, 1153 (1983).

<sup>2</sup> E. Lieb, T. Schultz, and D. Mattis, Annals of Physics **16**, 407 (1961).

<sup>3</sup> I. Affleck, T. Kennedy, E. H. Lieb, and H. Tasaki, Phys. Rev. Lett. **59**, 799 (1987).

<sup>4</sup> I. Affleck, T. Kennedy, E. H. Lieb, and H. Tasaki, Com-

munications in Mathematical Physics **115**, 477 (1988).

<sup>5</sup> X. Chen, Z.-X. Liu, and X.-G. Wen, Phys. Rev. B **84**, 235141 (2011).

<sup>6</sup> K. Wierschem and K. S. D. Beach, Phys. Rev. B **93**, 245141 (2016).

<sup>7</sup> Y.-Z. You, Z. Bi, A. Rasmussen, K. Slagle, and C. Xu,



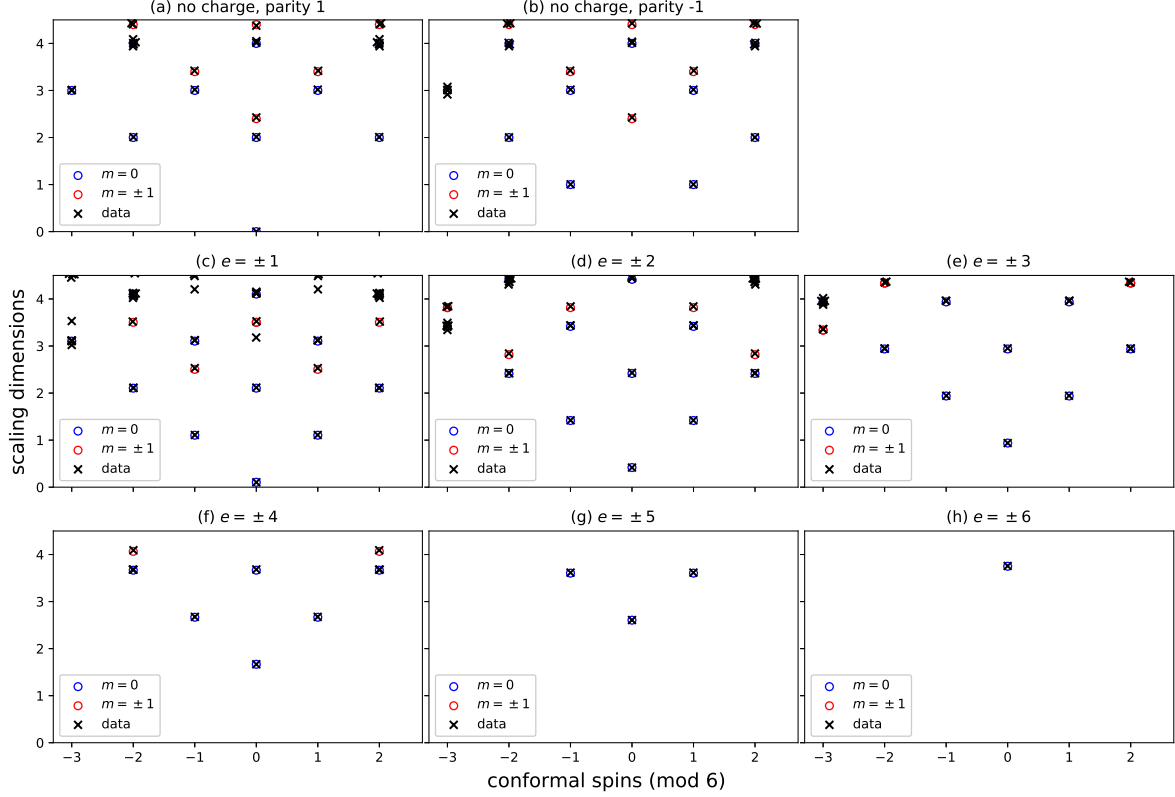


FIG. 40. The conformal tower at  $a_1 = .8, a_2 = 0$ , estimated from TNR at  $\chi = 26, \chi' = 16$ , after the twelfth coarse-graining step. We estimate  $g = 4.80 \pm 0.01$ .

- Phys. Rev. Lett. **112**, 247202 (2014).
- <sup>8</sup> T.-C. Wei, I. Affleck, and R. Raussendorf, Phys. Rev. Lett. **106**, 070501 (2011).
  - <sup>9</sup> T.-C. Wei and R. Raussendorf, Phys. Rev. A **92**, 012310 (2015).
  - <sup>10</sup> H. Niggemann, A. Klümper, and J. Zittartz, European Physical Journal B **13**, 15 (2000).
  - <sup>11</sup> Y. Hieida, K. Okunishi, and Y. Akutsu, New Journal of Physics **1**, 7 (1999).
  - <sup>12</sup> C.-Y. Huang, M. A. Wagner, and T.-C. Wei, Phys. Rev. B **94**, 165130 (2016).
  - <sup>13</sup> C.-Y. Huang and T.-C. Wei, Phys. Rev. B **93**, 155163 (2016).
  - <sup>14</sup> M. Levin and Z.-C. Gu, Phys. Rev. B **86**, 115109 (2012).
  - <sup>15</sup> L.-Y. Hung and X.-G. Wen, Phys. Rev. B **89**, 075121 (2014).
  - <sup>16</sup> F. D. M. Haldane, Phys. Rev. Lett. **61**, 1029 (1988).
  - <sup>17</sup> A. Garcia-Saez, V. Murg, and T.-C. Wei, Phys. Rev. B **88**, 245118 (2013).
  - <sup>18</sup> B. Bauer, G. Vidal, and M. Troyer, Journal of Statistical Mechanics: Theory and Experiment **2009**, P09006 (2009).
  - <sup>19</sup> D. Pérez-García, F. Verstraete, M. M. Wolf, and J. I. Cirac, Quantum Information & Computation **7**, 401 (2007).
  - <sup>20</sup> D. Pérez-García, F. Verstraete, M. M. Wolf, and J. I. Cirac, Quantum Information & Computation **8**, 650 (2008).
  - <sup>21</sup> J. C. Bridgeman and C. T. Chubb, Journal of Physics A Mathematical General **50**, 223001 (2017).
  - <sup>22</sup> N. Schuch, D. Pérez-García, and I. Cirac, Phys. Rev. B **84**, 165139 (2011).
  - <sup>23</sup> This cannot be done when the lattice is not bipartite; and in fact the choice of bond state in combination with the deformation breaks the  $SU(2)$  symmetry of the AKLT state down to  $\mathbb{Z}_2 \times \mathbb{Z}_2$  when the bond state is ferromagnetic.
  - <sup>24</sup> S. Singh, R. N. C. Pfeifer, and G. Vidal, Phys. Rev. A **82**, 050301 (2010).
  - <sup>25</sup> H. He, H. Moradi, and X.-G. Wen, Phys. Rev. B **90**, 205114 (2014).
  - <sup>26</sup> However, it is not guaranteed that the tensor will correspond to a true classical model as it may not contain strictly real, nonnegative entries.
  - <sup>27</sup> T. Nishino and K. Okunishi, Journal of the Physical Society of Japan **66**, 3040 (1997).
  - <sup>28</sup> R. Orús, Phys. Rev. B **85**, 205117 (2012).
  - <sup>29</sup> M. Levin and C. P. Nave, Phys. Rev. Lett. **99**, 120601 (2007).
  - <sup>30</sup> H. C. Jiang, Z. Y. Weng, and T. Xiang, Phys. Rev. Lett. **101**, 090603 (2008).
  - <sup>31</sup> Z.-C. Gu, M. Levin, and X.-G. Wen, Phys. Rev. B **78**, 205116 (2008).
  - <sup>32</sup> G. Evenbly and G. Vidal, Phys. Rev. Lett. **115**, 180405 (2015).
  - <sup>33</sup> P. Fendley, “A conformal field theory primer,” (2012), lecture notes available online.
  - <sup>34</sup> P. Francesco, P. Mathieu, and D. Sénéchal, *Conformal*

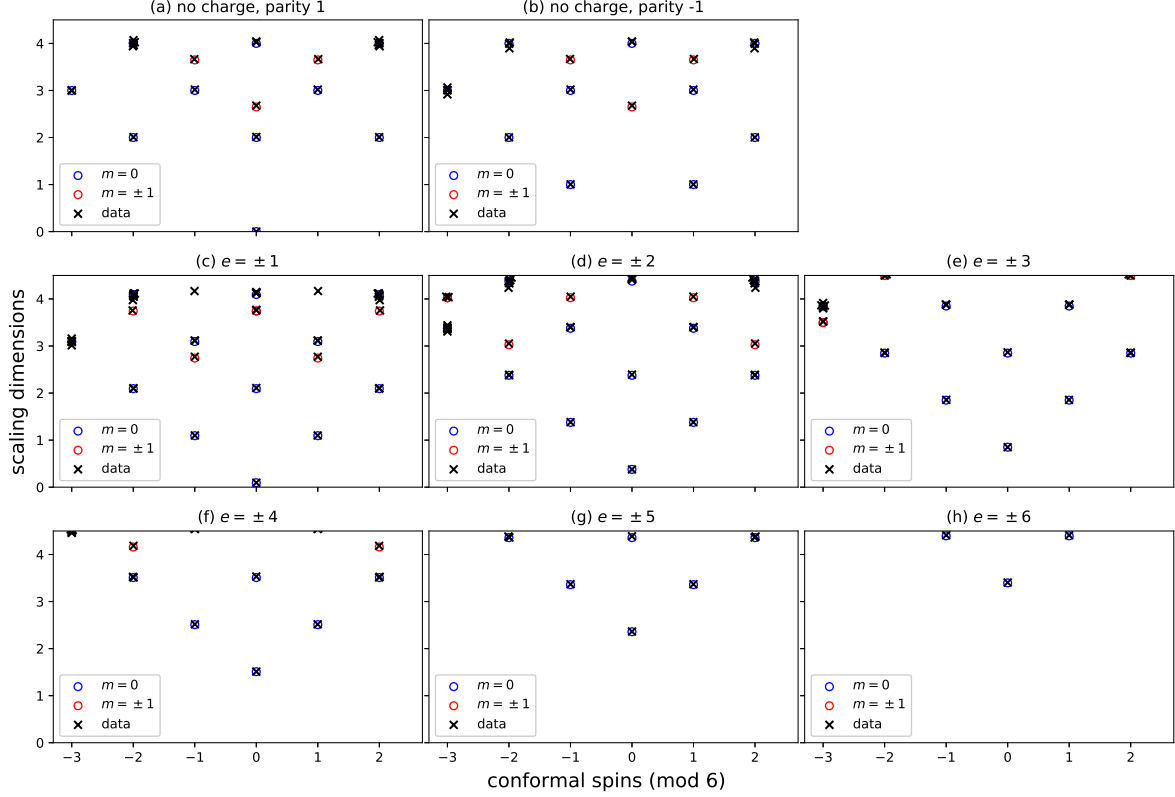


FIG. 41. The conformal tower at  $a_1 = .5, a_2 = .3$ , estimated from TNR at  $\chi = 26, \chi' = 16$ , after the twelfth coarse-graining step. We estimate  $g = 5.30 \pm 0.01$ .

*Field Theory*, Graduate Texts in Contemporary Physics (Springer New York, 2012).

<sup>35</sup> In the XY model, under the original approximation scheme of Kosterlitz and Thouless<sup>39</sup>,  $g = \frac{k_B T}{4\pi J}$ , based on the critical exponents they derive.

<sup>36</sup> A. Auerbach, *Interacting Electrons and Quantum Magnetism*, Graduate Texts in Contemporary Physics (Springer New York, 1998).

<sup>37</sup> Recall that our estimates of  $g$  are inversely proportional to our estimates of the first scaling dimension, determined from the logarithm of the ratio of the first two eigenvalues of the transfer matrix (or the first two with  $U(1)$  charges 0 and 1, respectively). Thus, when we observe the estimated value of  $g$  falling to 0 under coarse-graining, we can typically assume that this implies the opening of a gap. These cases should not be confused with actual free-boson CFTs with  $g < 1$ , which are equivalent to  $g > 1$  theories under T-duality, which exchanges “magnetic” vertex operators with “electric” operators and takes  $g \leftrightarrow 1/g$  - in which case the vertex operators with the least scaling dimension are now “magnetic” rather than “electric”.

<sup>38</sup> X. Chen, Z.-C. Gu, and X.-G. Wen, Phys. Rev. B **82**, 155138 (2010).

<sup>39</sup> J. M. Kosterlitz, Journal of Physics C: Solid State Physics **7**, 1046 (1974).

<sup>40</sup> R. J. Baxter, Journal of Statistical Physics **19**, 461 (1978).

<sup>41</sup> G. Evenbly and G. Vidal, Phys. Rev. Lett. **115**, 200401 (2015).

<sup>42</sup> C.-Y. Huang, T.-C. Wei, and R. Orús, Phys. Rev. B **95**, 195170 (2017).

<sup>43</sup> Z. Y. Xie, J. Chen, M. P. Qin, J. W. Zhu, L. P. Yang, and T. Xiang, Phys. Rev. B **86**, 045139 (2012).

<sup>44</sup> G. Evenbly, Phys. Rev. B **95**, 045117 (2017).

<sup>45</sup> M. Hauru, G. Evenbly, W. W. Ho, D. Gaiotto, and G. Vidal, Phys. Rev. B **94**, 115125 (2016).

<sup>46</sup> G. Evenbly and G. Vidal, Phys. Rev. Lett. **116**, 040401 (2016).

<sup>47</sup> J. L. Cardy, Nuclear Physics B **270**, 186 (1986).

<sup>48</sup> M. B. Hastings, Phys. Rev. Lett. **93**, 140402 (2004).

<sup>49</sup> M. B. Hastings and T. Koma, Communications in Mathematical Physics **265**, 781 (2006).

<sup>50</sup> S. Yang, Z.-C. Gu, and X.-G. Wen, Phys. Rev. Lett. **118**, 110504 (2017).

<sup>51</sup> J. Cardy, *Scaling and Renormalization in Statistical Physics*, Cambridge Lecture Notes in Physics (Cambridge University Press, 1996).

<sup>52</sup> The 2D irreps of both  $O(2)$  and  $D_{2N}$  are indexed by  $k$  (which corresponds to the absolute value of  $U(1)$  charge). An object that transforms under the representation  $k$  of  $O(2)$  for  $k < N/2$  also transforms under the representation  $k$  of its  $D_{2N}$  subgroup. We primarily use  $N = 40$ , where a general absence of  $k > 15$  irreps tells us that we should expect no  $k > 15$  irreps of  $O(2)$ , and in particular that the  $D_{2N}$  irreps which we do observe correspond exactly to the  $O(2)$  irreps with matching  $k$ .